Effective solar indices for ionospheric modeling: a review and a proposal for a real time regional IRI

A. Pignalberi[1], M. Pezzopane[2], R. Rizzi[1], and I. Galkin [3]

[1] Dipartimento di Fisica e Astronomia, Università di Bologna "Alma Mater Studiorum", Bologna, Italy.
[2] Istituto Nazionale di Geofisica e Vulcanologia, Rome, Italy.
[3] Space Science Laboratory, University of Massachusetts, Lowell, Massachusetts, USA

Corresponding author: Alessio Pignalberi (alessio.pignalberi2@unibo.it)

Key Points: Ionospheric data assimilation, International Reference Ionosphere, Universal Kriging, St. Patrick storm

Abstract

The first part of this paper reviews methods using effective solar indices to update a background ionospheric model focusing on those employing the Kriging method to perform the spatial interpolation. Then it proposes a method to update the IRI (International Reference Ionosphere) model through assimilation of data collected by a European ionosonde network. The method, called IRI UP (International Reference Ionosphere UPdate), that can potentially operate in real time, is mathematically described and validated for the period 9-25 March 2015 (a time window including the well-known St. Patrick storm occurred on 17 March), using IRI and IRTAM (IRI Real Time Assimilative Model) models as the reference. It relies on foF2 and M(3000)F2 ionospheric characteristics, recorded routinely by a network of 12 European ionosonde stations, which are used to calculate for each station effective values of IRI indices IG_{12} and R_{12} (identified as $IG_{12\text{eff}}$ and $R_{12\text{eff}}$); then, starting from this discrete dataset of values, two-dimensional (2D) maps of $IG_{12\text{eff}}$ and $R_{12\text{eff}}$ are generated through the universal Kriging method. Five variogram models are proposed and tested statistically to select the best performer for each effective index. Then computed maps of $IG_{12\text{eff}}$ and $R_{12\text{eff}}$ are used in the IRI model to synthesize updated values of foF2 and hmF2. To evaluate the ability of the proposed method to reproduce rapid local changes that are common under disturbed conditions, quality metrics are calculated for two test stations whose measurements were not assimilated in IRI UP, Fairford (51.7 N, 1.5 W) and San Vito (40.6 N, 17.8 E), for the storm-time option IRI, IRI UP, and IRTAM models. The proposed method turns out to be very effective under highly disturbed conditions, with significant improvements of foF2 representation and noticeable improvements of hmF2. Important improvements have been verified also for quiet and moderately disturbed conditions. A visual analysis of foF2 and hmF2 maps highlights the ability of the IRI UP method to catch small-scale changes occurring under disturbed conditions which are not seen by IRI.

1 Introduction

Prediction of solar and geomagnetic activity is essential for forecasting conditions in the near-Earth space environment in general and for ionospheric modelling and propagation processes in particular. This is an important subject of research in solar-terrestrial studies and significantly depends on types of solar events and their effects on the magnetosphere-ionosphere-atmosphere complex system (Zolesi and Cander 2014). It is a matter of fact that critical frequencies of ionospheric layers depend on measurable quantities related to solar radiation and to the neutral atmosphere composition and structure (Chapman 1930); at the same time, however,

the structure and dynamics of the ionosphere are profoundly dependent on measurable quantities related to geomagnetic activity (Buonsanto 1999).

Ionospheric empirical climatological models, like the International Reference Ionosphere (IRI) model (Bilitza et al. 2014), are not able to predict all the ionospheric variability, specifically under disturbed magnetic conditions (Mirò Amarante et al. 2007). IRI includes a storm option (Fuller-Rowell et al. 1998; Araujo-Pradere et al. 2002) which simulates the ionospheric plasma behavior under magnetically disturbed periods.
However, despite all the efforts made to improve the behavior of the IRI model under magnetically disturbed conditions, the response of the ionosphere under severe geomagnetic storms is still a challenge, as it was recently demonstrated by Pignalberi et al. (2016), who made a comparison between electron density values in the topside part of the ionosphere measured by Swarm satellites and calculated by IRI.

The aforementioned considerations lead to the conclusion that we need a model able to properly represent the ionospheric plasma variability caused by solar activity, geomagnetic activity and neutral atmosphere changes. To do this, according to the recent trend shown by the ionospheric community, it is necessary to complement climatological models with real-time space-sparse ionospheric measurements through a data assimilation scheme, as recently recognized by the IRI community (Bilitza et al. 2011, 2014).
Assuming there are several spatially-sparse ionospheric measurements, data assimilation is a process of merging measurements with a model to improve the estimate of the ionospheric conditions over the area covered by the model, also where direct measurements are not available. Thus, by means of data assimilation, it is possible to spatially expand the effectiveness of limited measurements using the model and, at the same time, to increase the accuracy of model estimates.
Several of the assimilating procedures used to update the IRI model are listed in Bilitza et al. (2011, 2014). In this work we review some of these methods, focusing on those using effective solar indices to update a climatological background and on Kriging methods.

This paper proposes a new assimilation method to update the IRI model in the European region. Specifically, foF2 and the propagation factor M(3000)F2 measurements are assimilated to calculate effective values of indices IG_{12} and R_{12} (called respectively IG_{12eff} and R_{12eff}) by taking into account that IRI uses the index IG_{12} to output foF2 values and the R_{12} index to output M(3000)F2 values. From these scattered values of IG_{12eff} and R_{12eff}, corresponding maps are generated by means of geostatistical interpolation called universal Kriging method; these maps are then used as input to the IRI model, thus obtaining updated values of foF2 and M(3000)F2, hence of hmF2. The method was tested on a period of time including the well-known and studied St. Patrick storm occurred on March 17 2015 (Astafyeva et al. 2015; Carter et al. 2016; De Michelis et al. 2016; Dmitriev et al. 2017; Nava et al. 2016; Nayak et al. 2016; Pignalberi et al. 2016; Spogli et al. 2016; Tulasi et al. 2016; Zhong et al. 2016). Its potentiality was statistically evaluated by comparing its output with that given by both the IRI model, with the storm option on, and the IRTAM (IRI Real Time Assimilative Model; Galkin et al. 2012) model.

Section 2 reviews methods using effective indices to update a background model and focuses on those employing the Kriging method to perform the spatial interpolation. Section 3 describes the data considered in this work and the method proposed to update IRI. Results and corresponding discussions are the subject of Sections 4, while conclusions are drawn in Section 5.

2 Effective solar indices and ionospheric empirical models updating methods: an historical and critical review

Empirical ionospheric models of the standard vertical incidence ionospheric characteristics are based on analytical spatial and temporal functions that oversimplify a number of processes that are instead important for radio communications applications. In these models ionospheric characteristics (such as foF2 and

$M(3000)$F2), the vertical electron density profile, and other ionospheric parameters as TEC (Total Electron Content), are represented as monthly median values varying as a function of geographic location, local time and solar activity. Models of this kind are then climatological since they are not designed to predict the day-to-day variability characterizing the ionospheric plasma. The major exponents of this category are global models as the IRI (Bilitza et al. 2014) and the NeQuick model (Nava et al. 2008), and regional models, for example the European SIRM (Zolesi et al. 1993) or the Chinese CRI model (Liu et al. 1994). Some models, like IRI, are provided with some options describing the behavior of some ionospheric characteristics under magnetically disturbed periods (Araujo-Pradere et al. 2002); nevertheless, these options are not able to catch very large deviations from climatology occurring under typical storms (Bradley et al. 2009).

2.1 Effective solar and ionospheric activity indices for modeling the ionosphere

To catch the ionospheric variability induced by solar activity, different solar and ionospheric activity indices have been used over the years. Solar activity indices are based on solar observations of phenomena occurring at the solar surface or atmosphere regardless of the effects that these phenomena can have on the ionospheric characteristics, and they are used simply as proxies. The most popular solar index is based on the long-term sunspot number measures that were used to define the daily Zurich sunspot number R and the twelve-months Zurich sunspot number running mean R_{12}, which is used in CCIR and URSI models encapsulated in the IRI model to model $M(3000)$F2. Other solar indices used in some ionospheric models are the F10.7 radio solar flux and the EUV solar emission flux.

The first ionospheric activity index, obtained by directly comparing a solar index with ionospheric measures, was the I_{F_2} index (Minnis 1955). It was obtained using monthly mean values of the Zurich sunspot number and monthly mean noon foF2 values recorded at three different ionospheric stations. Minnis (1955) assumed that the monthly mean of the Zurich sunspot number contains a principal component which has a one-to-one correlation with monthly mean noon foF2 values in an undisturbed ionosphere, and a residual component related to magnetic disturbances. He defined the I_{F_2} index in order to incorporate this principal component by means of a linear regression analysis between the two datasets of monthly mean values, considering magnetic disturbances as an error to be minimized.

The T index (Caruana 1990), developed by the Australian Ionospheric Prediction Service (IPS), is a development of the A index which was derived iteratively minimizing the linear regression's residuals between the R_{12} index and the average of the 24 hour monthly median values of foF2 as recorded at 16 stations. These monthly A indices obtained for every station were then used to calculate a global average A index. The definition of the T index extends this method by using all available ionospheric stations, which are grouped into many geographical sectors, to reduce the weight given to the data in regions rich of stations. Thus, the monthly T index for a region of the world is the weighted average of hourly T indices of the stations in that region.

Another directly calculated ionospheric activity index is the M_{F_2} index (Mikhailov and Mikhailov 1995). The ratio between foF2 and the magnetic factor M ($M = (\cos \chi_{\mathrm{MC}}/\cos \chi_{\mathrm{L}})^{\frac{1}{4}}$, where χ_{MC} is the solar zenith angle at the magnetically conjugate point of the F2 region and χ_L the local time one) is considered as a function of the cosine of the local solar zenith angle χ_{L}. The M_{F_2} index is defined as the average of foF2$/M$ values for which $\cos \chi$ minimizes the standard deviation of the foF2 versus M_{F_2} regression for each ionosonde station. The use of this index, instead of R_{12}, was demonstrated to improve the foF2 versus solar activity level regression by 30% for mid-latitudes and 10% for high-latitudes.

One of the most used ionospheric activity index is the IG index (Liu et al. 1983) and its twelve-months running mean IG_{12}. It is calculated from linear regression equations based on CCIR modeled monthly median foF2

values, at that time, dependent on R_{12}, and monthly medians foF2 values recorded at noon at 13 locations. The resulting index is the median of IG index values calculated in those selected locations, and the corresponding IG_{12} is used in CCIR and URSI to model foF2. Indices like IG, despite being calculated by means of a solar activity proxy, include also the variability caused by other phenomena affecting the ionosphere, like the geomagnetic activity, the neutral composition change or dynamical disturbances, because foF2 values, both measured and modeled, have these footprints. Thus, an index calculated merging available information deduced from measured and modelled ionospheric characteristics can tell us much more on ionospheric conditions than a direct solar activity index. This is the idea behind the development of effective indices made by several authors.

Secan and Wilkinson (1997) developed an effective sunspot number SSN_e by fitting a model of foF2 to observed foF2 values. Hence, SSN_e shares with IG index the concept of fitting a global model for foF2 to observations. The SSN_e index, deduced from a set of foF2 observations globally spread, is defined as the value that, when given as input to the URSI foF2 model, produces a weighted zero-mean difference between the observed and modeled foF2 values. In this formulation, every measured foF2 value is weighted according to the absolute value of the geomagnetic latitude and the local solar time. SSN_e values were demonstrated to catch more ionospheric variability compared to long-term solar activity indices, like R_{12} or IG_{12}, both for quiet and disturbed geomagnetic conditions. Thus, continuously updated indices have the potential to represent fast-time ionospheric variations, even though the global character of these indices does not allow to represent small-scale ionospheric variations.

A regionally-limited effective sunspot number was developed also by Zolesi et al. (2004) to real-time update the ionospheric European regional model SIRM (Simplified Ionospheric Regional Model) by means of vertical incidence measures collected by a network of digisondes. In this regard, real-time foF2 values measured at European stations are used to estimate an effective sunspot number, called R_{eff}, by comparing them with those predicted by SIRM, at the digisonde locations, by varying the R_{12} index (used as solar activity index in the SIRM model), and minimizing the corresponding mean square error. Hence, R_{eff} is the value that gives the minimum mean square error between modeled and measured foF2 values. This method turned out to make consistent improvements for both quiet and disturbed periods but only one value of R_{eff} is employed to predict the ionospheric variability over a large region (Belehaki et al. 2005). Using the SIRM model and measured $M(3000)$F2 values, Tsagouri et al. (2005) obtained new R_{eff} values but, in this case, with very poor results compared to those obtained using foF2 values.

It has been demonstrated (Mirò Amarante et al. 2007) that the ionosphere shows small-scale variations that global or regional empirical model describe hardly, especially for very disturbed periods. Therefore, ionospheric activity indices perform to their full potential if they are able to represent fast-time and small-scale ionospheric variations (assuming that slow-time and large-scale variations are sufficiently described by a global or regional model). In order to accomplish this task, such ionospheric indices should be quickly updated in time (one hour or less) and have a fine spatial structure. For this purpose, some attempts were made by several authors using different first-guess models (the most important of which are IRI and NeQuick models), ionospheric assimilated data (vertical ionospheric soundings made by ionosondes or GPS derived TEC values), and spatial interpolation methods (Kriging, spline, inverse weighted functions, natural neighbor).

A first approach to update the IRI model through updated indices was made by Komjathy and Langley (1996), who used hourly TEC maps with a 1°x1° spatial resolution. They were able to improve IRI-95 TEC outputs with an error reduction of about 32.5%. A similar approach was pursued by Hernandez-Pajares et al. (2002), who used 2-hourly TEC global maps, with a resolution of 5°x2.5° in longitude and latitude. They performed a local fit, over each IGS (International GPS Service) station (about 500 at that time), between IRI values and those of the TEC map by tuning the Sun Spot Number (SSN).

In order to improve the IRI predictions, Bilitza et al. (1997) used *fo*F2 measurements from more than 70 ionosondes worldwide, for the period 1986-1989, to calculate IG_{12} updated values. Index updates were calculated matching measured *fo*F2 values with those calculated by URSI model (Rush et al. 1989), for each station, and then were globally or zonally averaged. They found that zonally averaged updated indices bring to better results than globally ones, thus highlighting the importance of their spatial characterization.

Another approach, based on an IRI model updating using TEC values, was pursued by Barabashov et al. (2006). They used τ values ($\tau = TEC/NmF2$ is the equivalent slab thickness of the ionosphere) calculated by IRI and obtained by measured values of TEC and *fo*F2, to derive a $K = \tau(\text{obs})/\tau(\text{IRI})$ coefficient to be used to obtain an updated value of *fo*F2. They also modeled K coefficients taking into account that the largest contribution to differences between modeled and measured TEC can be ascribed to the topside part of TEC. Based on the results presented by the authors, their method turns out to be a good IRI updating method, specifically under disturbed periods, but is somewhat lacking on the spatial characterization.

Nava et al. (2005) applied a method similar to that proposed by Komjathy and Langley (1996) to the NeQuick model (Radicella and Leitinger 2001). Using hourly global TEC maps with a 2.5°x5° resolution (in latitude and longitude), they updated the NeQuick *effective ionization parameter Az* (normally calculated from the F10.7 solar activity index) by minimizing the difference between the experimental and the modeled vertical TEC. The authors obtained the best results at mid latitudes, specifically in the northern hemisphere, thus highlighting a general hemispherical asymmetry, and found a latitudinal dependence of the error magnitude. This would indicate a lower effectiveness of their method at low-latitudes (where the ionosphere shows a highly variable and complex dynamics), which could be ascribed to a lower data coverage and experimental data quality at these latitudes. Nevertheless, compared to the climatological F10.7 driven NeQuick model, the TEC updated NeQuick model improves TEC calculation by about 50%. NeQuick TEC-based updating was further developed by Nava et al. (2006) who updated Az values through a direct ingestion of GPS-derived slant TEC data in two different ways: using data from a single GPS receiver and using data from multiple ground stations. In the first method, one ground station tracks n GPS satellites calculating their respective slant TEC values, and an updated Az value is obtained after minimizing the root-mean square of the n measures. In the second method, an Az value is calculated for every station and then these scattered Az values are interpolated to obtain a regularly spaced grid by using an Inverse Weighting Function method in which the weight is the inverse of the square of the distance between the point and nodes. The two updating methods were shown to give clear improvements for both TEC and *fo*F2 values. Nava et al. (2011) introduced also a method to update *hm*F2 values given as output by the NeQuick model, by using *hm*F2 values extracted from Radio Occultation (RO) profiles. Using the Dudeney's formula that relates *fo*F2, *M*(3000)F2 and *hm*F2 (Dudeney 1983), implemented in NeQuick 2, they calculated the Az_hmF2 parameter minimizing the difference between RO-derived *hm*F2 values and NeQuick 2-derived *hm*F2 values.

A similar method was proposed by Migora-Orué et al. (2015), who assimilated global GPS-TEC maps into the IRI 2012 model, obtaining however small improvements during a high solar activity period for quiet days, and no improvement during a low solar activity period for quiet days.

The Nava et al. (2006) method has been recently employed by Olwendo and Cesaroni (2016) by assisting the NeQuick 2 model with vertical TEC (VTEC) measurements from a single GNSS station located in Kenya. These measurements are used to calculate the effective ionization level parameter (R_{12} in this case) which enables the difference between the measured and modeled VTEC over the station to be less or equal to 0.5 TECU. The method was evaluated comparing adjusted VTEC values with those measured in two nearby stations under years of low (2009) and moderate (2012) solar activity, proving to be very effective in either conditions. They also attempted to evaluate the effectiveness of the method by considering a more extended region of the central Africa (spanning from about 25°E÷50°E in longitude and 15°S÷20°N in latitude). In this

case some large model errors arose above all when points located far away by the assimilated station were considered, due to the very complex and highly variable behavior of the ionosphere at low latitudes.

An attempt to update the IRI model by means of measured GNSS TEC data collected in the African region has been recently pursued by Habarulema and Ssessanga (2016). They implemented an iterative procedure to minimize the difference between measured and modeled (by IRI 2012 model) TEC values modifying iteratively R_{12} and IG_{12} solar activity indices used by IRI to model the vertical electron density profile. This procedure is repeated for every GNSS station assimilated and then adjusted solar activity indices are averaged to obtain two single R_{12} and IG_{12} values which are used to update the IRI model. They evaluated their method for a disturbed (March 9 2012) and a quiet (March 25 2012) day comparing the corresponding output with both the ionosonde and radio occultation COSMIC derived data. By averaging results over the whole African region, the modified IRI 2012 gave an improvement of about 18% in estimating TEC during the stormy day, and about 28% during the quiet day. Anyway, the authors highlighted that the use of single averaged solar activity indices strongly smooth the spatial information embedded in them, above all considering a large and spatially variable region as is Africa.

TEC-based methods used to update IRI or NeQuick models suffer the limitation related to the calculation of TEC maps and measurements and to the intrinsic limit in height of these models. TEC maps and measurements have not yet reached an appropriate accuracy owing to noise, multipath propagation, phase jumps and subjectivity of the ionospheric model choice (being the calculation of vertical TEC values, derived from slant ones, dependent on the choice of the height of the ionospheric shell). Furthermore, models like IRI do not consider the plasmaspheric contribution, being the TEC calculation limited in height (2000 km), whilst GPS-based TEC measurements contain it (Klimenko et al. (2014) suggested that the plasmaspheric contribution to TEC values can potentially be up to 20% during the day and up to 50% at night), thus causing a mismatch which can degrade the accuracy of results regardless the employed updating method. These problems have been highlighted by Maltseva et al. (2010), who show that, in many cases, the direct ingestion of TEC values by IRI model leads to worse results compared to the assimilation of modeled τ (slab thickness) values (an argument raised also by Houminer et Soicher (1996) and Migora-Orué et al. (2015)). One of the main reasons of these discrepancies can be found in the fact that, in these models, TEC values are calculated a posteriori from the vertical electron density profile, while other characteristics as foF2 and M(3000)F2 are directly parametrized by the IRI model. Thus, an erroneous shape of the electron density profile (above all in the topside part, as recently demonstrated by Pignalberi et al. (2016)), can lead to an incorrect TEC estimate, even though the modeled foF2 value is improved through an updating procedure.

Ovodenko et al. (2015) have studied the possibility to update the IRI-2007 model calculating R_{12} updated values, for a single ionospheric station located in Kaliningrad (Russia), using two approaches: the first based on real-time slant TEC measurements by GNSS (as done by Nava et al. (2006)); the second based on foF2 measurements by ionosonde (as done by Bilitza et al. (1997)). In both approaches updated R_{12} indices are calculated in order to minimize the difference between IRI modeled values and measured ones, while the IG_{12} index is forced to be equal to R_{12} (which is a very limiting factor being these indices used by IRI to model different F2 layer characteristics, as it will be well described in section 3.2). For the analyzed cases, Ovodenko et al. (2015) found an important reduction of the error (about 70-80 %) using both approaches, compared to the climatological IRI-2007 model. They also found that the updating procedure based on slant TEC measurements is more effective for quiet geomagnetic conditions than for disturbed ones, and that the sunset is the most difficult period to represent, using both updated and non-updated IRI models.

2.2 Ionospheric modeling based on Kriging technique and assimilated data

The methods reported in the previous section focused principally on the choice of the best ionospheric parameters to constrain an activity index (solar or ionospheric), but considering the spatial description of lesser importance. Some of these effective indices, like SSN_e in Secan et al. (1997) and R_{eff} in Zolesi et al. (2004), are characterized by a single value which is considered valid for the whole area under study; others are estimated in all grid points of the assimilated ionospheric parameter map, like in Komjathy and Langley (1996) and Nava et al. (2005). In both cases, the spatial behavior of indices is overshadowed; the spatial description is delegated to the underlying climatological empirical model used or to the method used to obtain the assimilated map. In the case of a single index valid for the whole region, errors can arise due to an insufficiently accurate spatial description of the ionospheric parameters in the underlying empirical model. However, even assuming a perfect spatial description by the underlying model, errors arise because the effective indices contain inside them the imprint of several geophysical phenomena affecting the ionospheric parameter used in their computation, which are, in most cases, heavily spatially varying. Hence, it is clear the need to take into account the spatial behavior of an effective index. In the second case, that is the one of multiples indices calculated in each point of the region grid, errors can arise because the assimilated ionospheric parameter grid is itself obtained by means of interpolation of spatial scattered measures thus introducing additional errors that are difficult to estimate without a thorough a priori knowledge of how the assimilated grid was obtained. Hence, it is clear the need to take the full control on the spatial description of the effective indices through two main steps: 1) to obtain them from reliable measures taken in geographically scattered ionospheric stations; 2) to spatially interpolate the values obtained in 1) with a fully manageable spatial interpolation method, whose benefits and shortcomings can be clearly estimated and that can be adapted to the different geophysical conditions that can occur.

In an attempt to pursue both objectives, several spatial interpolation methods were developed to obtain an instantaneous mapping of several ionospheric parameters. Samardjiev et al. (1993) compared three spatial interpolation methods for an instantaneous ionospheric mapping of foF2 and M(3000)F2 characteristics over the European region, that is: the Inverse-distance power law method, the Minimum-curvature analysis and the geostatistical procedure known as Kriging method. This comparison showed that Kriging method gives the lowest mean square deviation for both small and large distances from the scattered assimilated measures, for both foF2 and M(3000)F2. The Kriging method will be discussed in the next section, being the spatial interpolation method used in this work. The description of the other interpolation methods is beyond the scope of this work, more information can be found in Davis (1986).

A Kriging method for an instantaneous mapping of foF2, was used in particular by Stanislawska et al. (1996a). They applied the ordinary Kriging method (Matheron 1963; Oliver and Webster 1990; Kitanidis 1997) to obtain foF2 maps in the European region after assimilating foF2 values measured by a network of 10 ionosondes. They described the spatial variation of the sampled data through a linear variogram model for which the nugget coefficient (the intercept of the straight line used to fit semivariance values) was zeroed by choosing the appropriate Scaling Factor value ($SF = dlon/dlat$, where $dlon$ and $dlat$ are the differences, in longitude and latitude respectively, for two different geographical points, describing the spatial anisotropy), with the sole slope of the straight line describing the whole spatial variation. They introduced also the concept of "ionospheric distance" for which the scaling factor (SF) is used to weight the ionospheric spatial anisotropy. This scaling factor was evaluated by Stanislawska et al. (1996a) for mid latitudes, and by Stanislawska et al. (1996b) for low and equatorial latitudes; it was found to vary from SF=0.8 at low and equatorial latitudes to SF=2 at mid-latitudes. To build the experimental variogram, and in order to have a consistent statistical sample, regardless of the hour of the day, they used foF2 values recorded for consecutive days, since semivariance values for a definite time moment were very randomly distributed. Anyhow, this way to proceed neglects any spatial correlation property linked to the ionospheric daily variability. This method was used also for an

instantaneous mapping of TEC by Stanislawska et al. (2002). Unfortunately, these works are not supported by any statistical validation and, with the proposed variogram's construction method, it turns out to be inapplicable for real-time applications in which only measures collected in a precise moment are available. Furthermore, several variogram models, i.e. several mathematical functions fitting the semivariance values in the experimental semivariogram, can be employed, each of them having different small-scale and large-scale properties (McBratney and Webster 1986). Limiting the analysis to only the linear variogram model is restrictive and may lead to less than optimal choices.

A Kriging method similar to that of Stanislawska et al. (1996a) is used by Liu et al. (2008) in conjunction with the CRI (China Reference Ionosphere) model, for the Chinese region. The authors probe different ionospheric values as input for the ordinary Kriging method, with a linear variogram model in which the nugget coefficient is zeroed by means of an appropriate choice of SF=2, that is: 1) $\left(fo\mathrm{F2}(x,y) - \overline{fo\mathrm{F2}(x,y)}\right)/\overline{fo\mathrm{F2}(x,y)}$, where $fo\mathrm{F2}(x,y)$ are values measured by a chinese network of ionosondes, and $\overline{fo\mathrm{F2}(x,y)}$ is the background calculated by the CRI model; 2) $fo\mathrm{F2}(x,y) - \overline{fo\mathrm{F2}(x,y)}$; 3) $fo\mathrm{F2}(x,y)$; 4) $R_{12}(x,y)$, the effective sunspot number inversely derived from $fo\mathrm{F2}(x,y)$ through the IRI model. The accuracy of the four proposed methods is evaluated, with a cross validation analysis that shows that method 1) provides best results because the information about physical gradients of electron density are retained using a background model, so that the accuracy and stability are increased in the regional reconstruction. Furthermore, they highlight an important difference between outer and inner regional stations and between low- and mid-latitude stations: best results are obtained for inner stations, as it is expected, and for mid-latitude stations owing to the difficulties of the CRI model to describe the northern crest of the equatorial anomaly.

Wang et al. (2010) investigated an approach similar to the method 1) proposed by Liu et al. (2008) for which the first step is to calculate an effective sunspot number R_{eff}, according to Zolesi et al. (2004), used to calculate an updated value of the I_{c} index (the solar activity index used by the CRI model, which quadratically depends on R_{12}), which is then used to obtain updated $fo\mathrm{F2}$ values with the CRI model. They statistically evaluated their method by means of a cross validation during two years of high solar activity and two years of minimum solar activity, after assimilating $fo\mathrm{F2}$ values from a network of nine Chinese ionosondes. They obtained a slight improvement with respect to the Liu et al. (2008) updating procedure, with a lower relative error for high solar activity than for low solar activity.

These results, although based on the CRI model, remain valid for any ionospheric model used as background in the updating procedure, regardless of the used approach. The goodness of results critically depends on the underlying background model and on its capability to catch the ionospheric variability, both spatially and temporally.

A Kriging method was applied by Orus et al. (2005) to improve the Technical University of Catalonia (UPC) global ionospheric maps (GIM) computed with GPS data. They used the ordinary Kriging method with an exponential variogram model, applied to the residuals between distributed UPC GIM TEC values and raw UPC GIM TEC values, in order to fulfill the stationary hypothesis with constant mean and standard deviation (Kitanidis 1997). Variograms were calculated considering two hours of data centered at even hours (0 UT, 2 UT, …, 22 UT) for small regions around each GIM grid point. The obtained variograms were then normalized obtaining a single variogram representing the whole map for these intervals of two hours (the need of considering several time periods to obtain the variogram is the same discussed by Stanislawska et al. (1996a)). They evaluated their method comparing it with previous UPC GIM and with IGS GIM maps for a self-consistency test, and with TEC data provided by TOPEX/Poseidon and JASON altimeter satellites. The self-consistency test showed that the root mean square of UPC Kriging GIM maps was about 16% lower than original UPC GIM maps, and about 3% lower than IGS GIM maps. Also, the comparison with

TOPEX/Poseidon and JASON TEC data showed that UPC Kriging GIM maps had better performance than original UPC GIM maps.

Regional ionosphere TEC mapping using the Kriging method was also investigated by Grynyshyna-Poliuga et al. (2014), who used IGS TEC values recorded by 15 stations located in the European region to reconstruct TEC maps by means of the ordinary Kriging method. They probed the opportunity to use different stationary variogram models, in particular spherical, exponential and gaussian. They considered 15-minutes TEC values during three days including a geomagnetic storm, obtaining maps in a region located between 30°N-60°N in latitude and 40°W-45°E in longitude on a 2.5°x2.5° grid. These maps could properly represent significant features of the ionosphere response, as latitudinal variations of the ionospheric trough for disturbed conditions, but the authors did not make any statistical validation of both the method and the stationary variogram that performed better.

The aforementioned considerations about the application of the ordinary Kriging method to generate ionospheric parameters maps led us to conclude that it might be a good spatial interpolation method. However, it is characterized by several user arbitrary choices (the variogram to be used, which and how many values to be used to build it, use of all values or only a spatial selection of it, …) that make its use "dangerous", in the sense that certain choices provide worse results than other, more user-friendly, interpolation methods. In the following section, the universal Kriging method will be described, since the authors consider it more suitable than the ordinary one for ionospheric issues. Several stationary and non-stationary variogram models will be investigated, in order to make the most of the potentiality of the Kriging method.

2.3 Five steps to make a good ionospheric model update based on solar indices

The critical review of previous sections highlights five points to be followed in the development of a method to generate reliable ionospheric maps:

1. An empirical climatological ionospheric model is adopted with improved temporal and spatial description of the ionosphere, and whose ionospheric characteristics depend on some solar/ionospheric activity indices that can be chosen by the user;
2. The most reliable ionospheric characteristics must be assimilated, in order to have the highest confidence. Specifically, those characteristics that are directly parametrized by the underlying model, preferably those depending on only one solar/ionospheric activity index, should be considered;
3. The assimilated ionospheric characteristic is used to update the solar/ionospheric activity index by which it depends, for several points on a chosen region;
4. A spatial interpolation method is used to obtain maps of updated solar/ionospheric activity index/indices on a region whose extension depends on the geographical position of stations from which data are assimilated;
5. The underlying model is fed with the updated solar/ionospheric activity index/indices to obtain updated values of the selected ionospheric characteristics.

The choices we have made to build our model, strictly linked to the aforementioned five points, are also guided by the considerations made in the previous section about potentialities and shortcomings of each developed method. Details will be provided in the following section.

3 Data and method

3.1 Data

The considered period is the one between the 9 March 2015 at 00 UT (Universal Time) and the 25 March 2015 at 23 UT, a time period including the so-called St. Patrick geomagnetic storm, the most intense geomagnetic

storm observed during solar cycle 24, classified as severe and for which the Kp index reached the maximum value of 8. The sudden storm commencement was observed from ground observatories on 17 March 2015 at around 04:45 UT with the arrival at the Earth of a Coronal Mass Ejection. The storm reached its maximum intensity on 17 March at around 23:00 UT and it was characterized by a minimum value of the D_{st} index of −223 nT. The considered time period was characterized initially by a magnetically quiet period, as it is shown by the D_{st} and AE values close to zero (see the bottom panel of Fig. 4), lasting until the sudden storm commencement occurred on 17 March 2015 at about 05 UT. Then, a strongly magnetically disturbed period characterizes the main phase of the storm, from the sudden storm commencement until the end of 18 March 2015, for which the D_{st} index becomes deeply negative and the AE index increase significantly its value. Hence, a long recovery phase characterizes the days until the end of the studied period, for which the D_{st} index slowly increases to zero, while the AE index is still characterized by several perturbations due to sub-storms.

Hourly values of foF2, M(3000)F2, hmF2 and foE (the critical frequency of the E region) are used in this work. These data were downloaded from the DIDBASE (Digital Ionogram DataBASE) (Reinisch and Galkin 2011) by means of the SAO Explorer software, developed by the University of Massachusetts, Lowell. Fourteen ionospheric stations in the European sector, from 15°E to 45°W in longitude and from 30°N to 60°N in latitude, are considered (see Table 1). Two of these stations, specifically Fairford and San Vito, have been used only as test sites to verify the model performance. The two test stations are well spaced in latitude, to test the different effects of the geomagnetic storm at different latitudes. Furthermore, the Fairford station is located near Chilton station, while San Vito station is relatively isolated and surrounded by Rome, Gibilmanna and Athens stations, therefore they experiment different boundary conditions. The quality of the downloaded ionograms have been verified by selecting only those with a C-score > 75 (for more information on C-score see http://www.ursi.org/files/CommissionWebsites/INAG/web-73/confidence_score.pdf), for the stations equipped with the ARTIST software (Galkin et al. 2008), while those recorded by stations equipped with Autoscala software (Pezzopane and Scotto 2005) have been visually verified.

Table 1 Ionospheric stations from which data are assimilated with corresponding geographical coordinates, type of ionosonde and autoscaling software. Station names in bold are used only as test stations, and data are not assimilated.

Ionospheric stations	Lon (degrees)	Lat (degrees)	Ionosonde type	Autoscaling software	State
Athens	23.5 E	38.0 N	Digisonde DPS-4D	Artist 5	assimilated
Chilton	0.6 W	51.5 N	Digisonde DPS-1	Artist 4	assimilated
Dourbes	4.6 E	50.1 N	Digisonde DPS-4D	Artist 5	assimilated
El Arenosillo	6.7 W	37.1 N	Digisonde DPS-4D	Artist 5	assimilated
Fairford	1.5 W	51.7 N	Digisonde DPS-4D	Artist 5	Used as test data
Gibilmanna	14.0 E	37.9 N	AIS-INGV	Autoscala 4.1	assimilated
Juliusruh	13.4 E	54.6 N	Digisonde DPS-4D	Artist 5	assimilated
Moscow	37.3 E	55.5 N	Digisonde DPS-4	Artist 5	assimilated
Nicosia	33.2 E	35.0 N	Digisonde DPS-4D	Artist 5	assimilated
Pruhonice	14.6 E	50.0 N	Digisonde DPS-4D	Artist 5	assimilated
Rome	12.5 E	41.8 N	AIS-INGV	Autoscala 4.1	assimilated
Roquetes	0.5 E	40.8 N	Digisonde DPS-4D	Artist 5	assimilated
San Vito	17.8 E	40.6 N	Digisonde DPS-4D	Artist 5	Used as test data
Warsaw	21.1 E	52.2 N	VISRC2	Autoscala 4.1	assimilated

3.2 Effective index calculation

In the method we are describing, the model used as background is the IRI model, because it has all the features highlighted at point 1. of section 2.3.

IRI is an empirical climatological standard model of the ionosphere. It is an international project sponsored by the Committee on Space Research (COSPAR) and the International Union of Radio Science (URSI). The major data sources are the worldwide network of ionosondes, the powerful incoherent scatter radars, some topside sounders, and in situ instruments flown on many satellites and rockets. The IRI model, for a given location, time and date, provides monthly averages of several ionospheric hourly quantities, on the base of solar, magnetic and ionospheric indices.

IRI includes a storm-model option (Fuller-Rowell et al. 1998; Araujo-Pradere et al. 2002), which simulates the ionospheric plasma behavior under magnetically disturbed periods, operating on *fo*F2, *hm*F2 and *fo*E and on the topside part of the vertical electron density profile. The storm-model option for *fo*F2 is based on a large number of storms (in the time period 1980-l990) and the ratio between disturbed and quiet *fo*F2 values was modelled by means of a proxy calculated as the integral of the magnetic index a_p over the previous 33 hours, with a weighting function deduced from a regression analysis based on a physically based modeling. The storm-model is able to capture the main feature of the ionospheric storm response, which is the deep ion depletion ("negative phase") that typically develops in the summer hemisphere during the driven phase of a storm and persists well into the recovery phase (Bilitza 2003).

Araujo-Pradere et al. (2003) evaluated the IRI storm option by considering all storms occurred in 2000 and 2001 (14 in total) and by analyzing the response seen at over 30 ionosonde stations. They found that during storm periods the IRI storm-option gives a 30% improvement with respect to the IRI model, and it is able to capture more than 50% of the variability due to the storm, but results are greatly dependent on the season, being good in summer and equinoctial months, but of lesser quality in winter.

IRI modeling of F2 layer characteristics, *fo*F2 and *M*(3000)F2, relies on CCIR and URSI long-term global maps; users can choose between these two options, or give their own values of *fo*F2 or *M*(3000)F2. CCIR maps are based on a procedure of numerical mapping pioneered by Jones and Gallet (1962) and Jones et al. (1969). URSI maps make use of the same CCIR mapping procedure, including a number of synthesized data points based on the thermospheric wind theory, as explained by Rush et al. (1989). URSI maps try to overcome the limitations of CCIR maps due to the geographical coverage of assimilated measurements, mainly located in the Northern hemisphere and without coverage of ocean areas.

In either mapping procedures diurnal/spherical harmonic expansions are used to represent the diurnal cycle of *fo*F2 and *M*(3000)F2, and the corresponding diurnal variation is based on a Fourier analysis of the monthly median diurnal variation as observed by a worldwide network of ionosondes used as database (for solar minimum years 1954, 1955 and 1964, and solar maximum years 1956-1958). The general form of the numerical map function $\Omega(\lambda, \theta, T)$ (Ω is either *fo*F2 or *M*(3000)F2, $\lambda \in [-90,90]$ is the geographic latitude, $\theta \in [0,360)$ is the East geographic longitude, and $T \in [-180,180)$ is the Universal Time (UT) expressed as an angle) is (ITU-R 2009):

$$\Omega(\lambda, \theta, T) = a_0(\lambda, \theta) + \sum_{j=1}^{H} \left[a_j(\lambda, \theta) \cos jT + b_j(\lambda, \theta) \sin jT \right], \tag{1}$$

where H is the maximum number of harmonics used to represent the diurnal variation ($H = 6$ for *fo*F2; $H = 4$ for *M*(3000)F2).

The diurnal expansion Fourier coefficients a_0, a_j, b_j vary with geographic coordinates and this variation is captured in the spatial spherical expansion over the geographic latitude and longitude:

$$a_0(\lambda, \theta) = \sum_{k=0}^{K} U_{0,k} G_k(\lambda, \theta), \tag{2a}$$

$$a_j(\lambda, \theta) = \sum_{k=0}^{K} U_{2j,k} G_k(\lambda, \theta) \qquad j = 1,2,\ldots,H, \tag{2b}$$

$$b_j(\lambda, \theta) = \sum_{k=0}^{K} U_{2j-1,k} G_k(\lambda, \theta) \qquad j = 1,2,\ldots,H, \tag{2c}$$

where K is the highest harmonic order used in the spherical expansion that determines the number of coefficients used in longitude ($K = 9$ for both foF2 and M(3000)F2).

The $G_k(\lambda, \theta)$ terms contain the 2-D "geographical" expansion basis functions, optimized for representation of foF2 by using power sine functions of modip, power cosine of latitude, and longitudinal harmonics (for more details see ITU-R (2009)). The maximum order K=76 is selected to resolve the smallest spatial scale size of the ionospheric climate variability, which detail will be at times insufficient for representing the real-time ionosphere. Increasing the order K for nowcasting applications as to provide a finer detail of the spatial resolution, however, is limited by several practical considerations, including instrument data noise. As Bradley et al. (2009) argued, no advantage would have been gained by considering a higher order leading to a smaller scale size, because the order of the expansion is strictly linked to the spatial instrument coverage. CCIR maps are recommended for mainly land regions, whilst URSI maps when the mapping area includes large ocean areas. In our study CCIR maps are considered.

Thus IRI needs 13 diurnal × 76 spherical = 988 coefficients to globally represent the foF2 (9 diurnal × 49 spherical = 441 coefficients for M(3000)F2) diurnal variation of a definite month. These arguments are repeated for every month and for two selected levels of solar activity ($IG_{12} = 0$ and $IG_{12} = 100$ for foF2, $R_{12} = 0$ and $R_{12} = 100$ for M(3000)F2); thus, the total number of stored coefficients that are used by the IRI model to obtain foF2 for any given time and location is 988×12 months × 2 levels of solar activity = 23,712 coefficients (441×12 months × 2 levels of solar activity = 10,584 coefficients for M(3000)F2).

The IRI model assumes that these coefficients are linearly correlated with solar activity proxies (direct proportionality between IG_{12} and foF2, reverse proportionality between R_{12} and M(3000)F2), until a threshold value set to 150 (for both indices) beyond which both foF2 and M(3000)F2 are kept constants, to account for the well-known ionospheric saturation effect. Thus, these coefficients can be described by formulas (Komjathy and Bradley 1996):

$$U_{2j,k} = \left[U_{2j,k}^{\mathrm{low}} \left(1 - \frac{IG_{12}}{100} \right) + U_{2j,k}^{\mathrm{high}} \frac{IG_{12}}{100} \right], \tag{3a}$$

$$U_{2j-1,k} = \left[U_{2j-1,k}^{\mathrm{low}} \left(1 - \frac{IG_{12}}{100} \right) + U_{2j-1,k}^{\mathrm{high}} \frac{IG_{12}}{100} \right], \tag{3b}$$

for foF2, and

$$U_{2j,k} = \left[U_{2j,k}^{\mathrm{low}} \left(1 - \frac{R_{12}}{100} \right) + U_{2j,k}^{\mathrm{high}} \frac{R_{12}}{100} \right], \tag{4a}$$

$$U_{2j-1,k} = \left[U_{2j-1,k}^{\mathrm{low}} \left(1 - \frac{R_{12}}{100} \right) + U_{2j-1,k}^{\mathrm{high}} \frac{R_{12}}{100} \right], \tag{4b}$$

for $M(3000)F2$, with the specification that $U_{2j,k}(IG_{12} \text{ or } R_{12} > 150) = U_{2j,k}(IG_{12} \text{ or } R_{12} = 150)$ and $U_{2j-1,k}(IG_{12} \text{ or } R_{12} > 150) = U_{2j-1,k}(IG_{12} \text{ or } R_{12} = 150)$.

In formulas (3)-(4) $U_{2j,k}^{low}$ and $U_{2j,k}^{high}$ (similarly for 2j-1 terms) are the coefficient values calculated for IG_{12} or R_{12} equal to 0 (low solar activity) and equal to 100 (high solar activity), respectively.

IRI calculates hmF2 through the empirical formula (Bilitza et al. 1979):

$$hmF2(\text{km}) = \frac{1490}{(M(3000)F2 + DM) - 176}, \tag{5a}$$

where the correction factor DM is

$$DM = \frac{f_1 f_2}{\left(\frac{foF2}{foE} - f_3\right) + f_4}, \tag{5b}$$

and the solar activity functions are

$$f_1 = 0.00232 R_{12} + 0.222, \tag{5c}$$

$$f_2 = 1 - \frac{R_{12}}{150 e^{-\left(\frac{\psi}{40}\right)^2}}, \tag{5d}$$

$$f_3 = 1.2 - 0.0116 e^{\frac{R_{12}}{41.84}}, \tag{5e}$$

$$f_4 = 0.096 \frac{R_{12} - 25}{150}, \tag{5f}$$

where ψ is the magnetic dip latitude.

hmF2 is then explicitly dependent on R_{12}, through f_1, f_2, f_3 and f_4, but, at the same time, is also implicitly dependent on R_{12} through $M(3000)F2$ (as mentioned earlier) and foE (as it will be shown). The presence of foF2 in the DM factor makes hmF2 implicitly dependent also on IG_{12}.

In the CCIR model used by IRI, foE is given by (Bilitza 1990):

$$foE^4 = A \cdot B \cdot C \cdot D. \tag{6}$$

The four factors A, B, C, D in Eq. (6) depend on the 12-months running mean (COV_{12}) of the $F_{10.7}$ solar flux. IRI estimates COV_{12} from R_{12} values through the formula:

$$COV_{12} = 63.75 + R_{12}(0.728 + R_{12} \cdot 0.00089). \tag{7}$$

Thus, foE values depend on R_{12} values.

IRI gives the user the opportunity to input a value for both R_{12} and IG_{12}. In this way, using real-time updated IG_{12} and R_{12} values, improved foF2 and $M(3000)F2$ values can be obtained. This is because the IRI model for the current time uses forecasted values of IG_{12} and R_{12}. Moreover, IG_{12} and R_{12}, being 12-months running means, are strongly smoothed proxies that are good to model long-term variations of the ionosphere but cannot catch short-term phenomena, like those caused by geomagnetic storms. IRI, of course, is a climatological

model, so we do not expect that phenomena occurring at shorter time scale, like for instance those characterizing geomagnetic disturbed conditions, are reliably predicted by the model. At the same time, however, because the ionospheric characteristics associated to the two anchor points of the IRI vertical electron density profile (the E and F2 peaks) are modelled through the use of these two indices, we would expect that feeding the model with updated IG_{12} and R_{12} indices could make the model sensitive also to the short-term variability, which is now included in the indices. In addition, IG_{12} and R_{12} indices are global, thus they do not catch geographical variations that are commonly observed in several ionospheric phenomena, leaving the description of these to the spherical harmonic analysis or to other functions, as it was previously seen.

In our model, values of foF2 (for $IG_{12} = 0$ and 100) and $M(3000)$F2 (for $R_{12} = 0$ and 100) are calculated by IRI at each of the assimilated ionospheric stations listed in Table 1. The two values are used to linearly interpolate foF2 vs IG_{12} and $M(3000)$F2 vs R_{12} over a large range of values. An example is shown in the upper panel of Fig.1 for the Athens station on March 9 2015 at 17 UT, for IG_{12}.
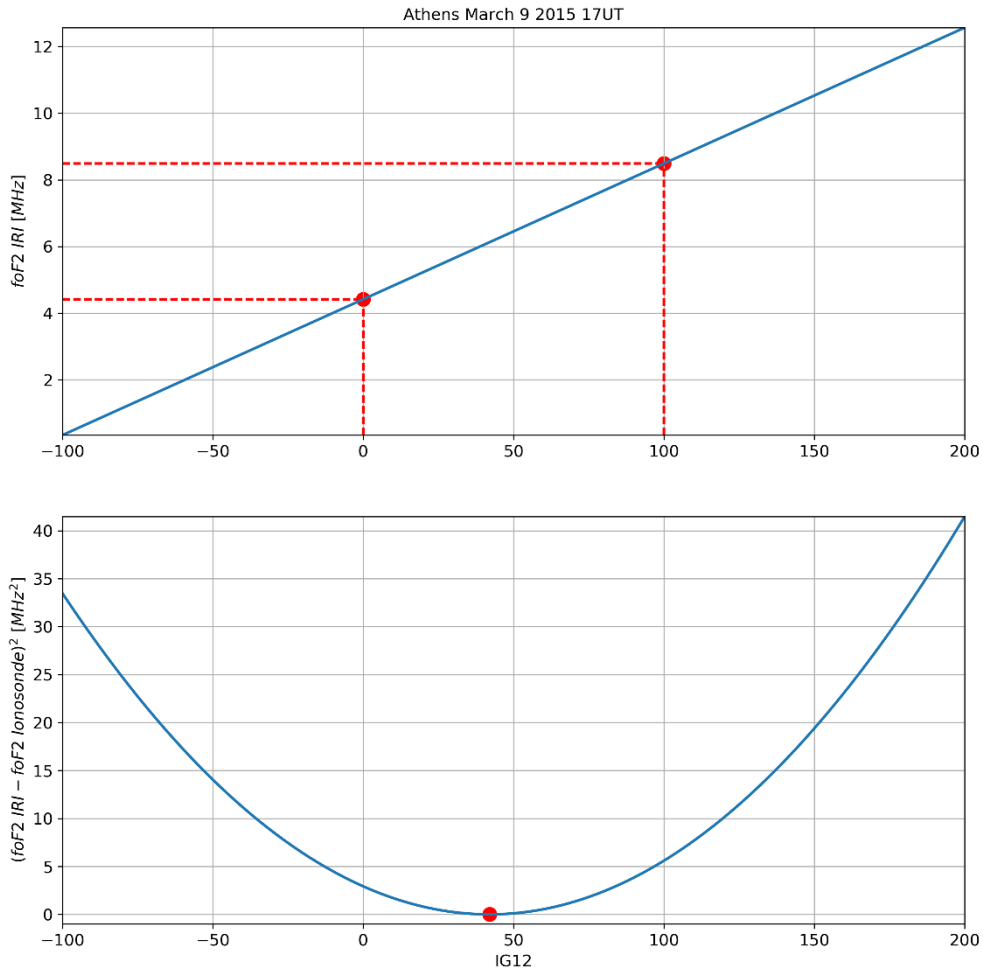
Fig. 1 Linear fit between foF2 and IG_{12} values (upper panel). Two red points represent the IRI simulated foF2 values for $IG_{12} = 0$ and $IG_{12} = 100$. Plot of the square difference between observed and modeled values of foF2 vs IG_{12} (lower panel). Red point is the calculated minimum which corresponds to the effective values of IG_{12}.

The square difference between observed and modeled values of foF2 and $M(3000)$F2 is calculated, for every station, according to following formulas:

$$\Delta_{IG_{12}} = (fo\text{F2}_{\text{obs}} - fo\text{F2}_{\text{IRI}}(IG_{12}))^2, \tag{8a}$$

$$\Delta_{R_{12}} = \left(M(3000)\text{F2}_{\text{obs}} - M(3000)\text{F2}_{\text{IRI}}(R_{12})\right)^2; \tag{8b}$$

$fo\text{F2}_{\text{obs}}$ and $M(3000)\text{F2}_{\text{obs}}$ are the observed values, and $fo\text{F2}_{\text{IRI}}(IG_{12})$ and $M(3000)\text{F2}_{\text{IRI}}(R_{12})$ are the corresponding modeled values, represented by the linear fits shown in the upper panel of Fig.1. An example is shown in the lower panel of Fig.1. The square difference functions expressed by (8) are parabolas for which it is simple to find the minimum corresponding to the effective values of IG_{12} and R_{12}.

Since values of $IG_{12\text{eff}}$ and $R_{12\text{eff}}$ are calculated for each assimilated station, an interpolation of these through the chosen grid is needed. To accomplish this task, the universal Kriging method is considered to obtain maps of $IG_{12\text{eff}}$ and $R_{12\text{eff}}$ (point 4. of Section 2.3).

3.3 Kriging interpolation method

The Kriging method is an advanced geostatistical procedure that, used as an interpolator, generates an estimated surface from a scattered set of punctual geophysical measurements (Matheron 1963; Oliver and Webster 1990; Kitanidis 1997).

It belongs to statistical *BLUE* (Best Linear Unbiasedness Estimation) methods, for which the first two statistical moments of the random field, which are the *mean function* (first moment) and the *covariance function* (second moment), are used to select the best estimation method. Thus, the model of the spatial structure consists of mathematical expressions chosen to describe the mean function and the covariance function.

Given n measurements of the variable z at locations with spatial coordinates $\boldsymbol{x}_1, \boldsymbol{x}_2, \ldots, \boldsymbol{x}_n$, Kriging estimates the value of z at point $\boldsymbol{x}_0$, making a linear combination of measurements (Oliver and Webster 1990):

$$\hat{z}_0 = \sum_{i=1}^{n} \lambda_i z(\boldsymbol{x}_i). \tag{9}$$

Thus, the problem is reduced to select a set of coefficients $\lambda_1, \ldots, \lambda_n$ that match the conditions of *unbiasedness* ($E[\hat{z}_0 - z(\boldsymbol{x}_0)] = 0$, the expected value of the difference between the Kriging estimate $\hat{z}_0$ and the actual value $z(\boldsymbol{x}_0)$, i.e. the *estimation error*, must be zero) and of *minimum variance* (the mean squared estimation error $E[(\hat{z}_0 - z(\boldsymbol{x}_0))^2]$ must be minimum).

Eq. (9) highlights how Kriging is a global interpolation method. Global interpolation methods use a weighted sum of all data to compute output values, thus the information contained in each measured point is shared with all other points, regardless the distance between two points, taking into account that the spatial correlation between points is embedded in the measured data itself.

3.3.1 The experimental variogram

The building of the *experimental variogram* (or semivariogram) is the core of the Kriging method, because it allows to investigate the spatial correlation between measurements, and is the first step of the structural analysis (McBratney and Webster 1986, Kitanidis 1997). Consider we have n measurements $z(\boldsymbol{x}_1), z(\boldsymbol{x}_2),\ldots, z(\boldsymbol{x}_n)$,

and plot the squared difference $\frac{1}{2}[z(\boldsymbol{x}_i) - z(\boldsymbol{x}_i')]^2$ (which is the *semivariance* $\gamma(h_i)$, where index *i* refers to each pair of measurements $z(\boldsymbol{x}_i)$ and $z(\boldsymbol{x}_i')$) against the distance $h_i = |\boldsymbol{x}_i - \boldsymbol{x}_i'|$ for all measurement pairs (where | | means the length of a vector). Hence, for *n* measurements there are $\frac{n(n-1)}{2}$ pairs that form a scatter plot which is the experimental variogram.

Hence, considering the summation over the index *i*, the *semivariance* is defined as (Oliver and Webster 1990):

$$\gamma(h) = \frac{1}{2n}\sum_{i=1}^{n}[z(\boldsymbol{x}_i) - z(\boldsymbol{x}_i')]^2. \tag{10}$$

It can be demonstrated that the semivariance is equal to minus the **covariance** function plus a constant, where the constant is the variance (Kitanidis 1997):

$$\gamma(h) = -R(h) + R(0) = -R(h) + \sigma^2. \tag{11}$$

The experimental variogram contains information about the *scale of fluctuations* of the variable: the behavior of the experimental variogram near the origin indicates variability at small scale while the behavior of the experimental variogram at large distances is indicative of the large-scale behavior.

3.3.2 Variogram models

The second step of the structural analysis is to fit a mathematical expression, called *variogram model*, to the points of the experimental variogram. Variogram models are linear combinations of simple mathematical functions with the restriction that these should be positive definite.

Considering their large-scale behavior, variogram models can be grouped in two distinct families: *stationary* and *non-stationary* models. Stationary models manifest small-scale fluctuations, compared to the size of the domain, around some well-defined mean value; the corresponding experimental variogram should stabilize around a value, called *sill,* and the length scale at which the sill is obtained, called *range* or *correlation length*, describes the scale at which two measurements of the variable become practically uncorrelated. Variograms of non-stationary models increase even at distances comparable to the maximum separation of interest.

The behavior of the variogram for short distances determines whether the spatial function appears continuous and smooth. Three different small-scale behaviors are identifiable: *discontinous*, *parabolic*, and *linear*. A variogram is discontinuous if the average sampling interval (i.e., the distance between measurement locations) is several times larger than the scale of fluctuations of the variable; in this case, two adjacent values are about as different as two distant values. At the scale of the sampling interval, the variable *z* is discontinuous because it changes abruptly from one sampling point to the next. In this case, the experimental variogram is approximately a straight horizontal line, and since it doesn't converge to zero as the separation decreases, there is a discontinuity of the experimental variogram at the origin, or a *nugget effect* (a condition called *microvariability*). Instead, if all the variability is at a scale much larger than that of the sampling interval, changes of values are so gradual that both *z* and its slope vary continuously. In this case, the experimental variogram has a parabolic behavior near the origin, that is, it is proportional to h^2 for small values of *h*. An intermediate case is when the variable presents most of its variability at a scale larger than the average sampling interval, but also some variability at a scale comparable to that of the measurement spacing; in this case, changes of *z* between adjacent sampling points are gradual so that *z* is practically continuous at the scale of measurements, and the experimental variogram has approximately a linear behavior near the origin, that is, the variogram is proportional to *h* for small values of *h*.

Five different variogram models are used in this work (Kitanidis 1997): *gaussian*, *spherical* and *exponential*, that are stationary models; *power* and *linear*, that are non-stationary models.

- Gaussian:

$$\gamma(h) = c_0 + (\sigma^2 - c_0)\left(1 - e^{-\left(\frac{7h}{4\alpha}\right)^2}\right),\tag{12}$$

where c_0 is a constant, called *nugget value*, σ^2 is the *sill* and α is the *range*. The gaussian model has a parabolic behavior at the origin.

- Spherical:

$$\gamma(h) = \begin{cases} c_0 + (\sigma^2 - c_0)\left(\dfrac{3}{2}\dfrac{h}{\alpha} + \dfrac{1}{2}\left(\dfrac{h}{\alpha}\right)^3\right) & for \ \ 0 \le h \le \alpha, \\ \sigma^2 & for \ \ h > \alpha. \end{cases}\tag{13}$$

The spherical model exhibits a linear behavior at the origin.

- Exponential:

$$\gamma(h) = c_0 + (\sigma^2 - c_0)\left(1 - e^{-\left(\frac{3h}{\alpha}\right)}\right).\tag{14}$$

The exponential model exhibits a linear behavior at the origin.

- Power:

$$\gamma(h) = c_0 + \theta h^s,\tag{15}$$

where $\theta > 0$ is the *scale* and $0 < s < 2$ is the *exponent*.

- Linear:

$$\gamma(h) = c_0 + \theta h,\tag{16}$$

where $\theta > 0$ is the *slope*.

Examples of variogram models defined by formulas (12)-(16) are shown in Fig. 2. All variograms of Fig. 2 have the same nugget value (this is testified by the same intercept of all curves), and stationary models are considered with the same sill and range values. Figure 2 shows clearly the different large-scale behavior between non-stationary and stationary models. It is worth noting that stationary models present a different small-scale behavior, also considering same values of both range and sill. In particular, the gaussian model is the smoothest one and reaches the sill value well beyond the range value; instead, exponential and spherical models are steeper near the origin and reach the sill value near the range value.
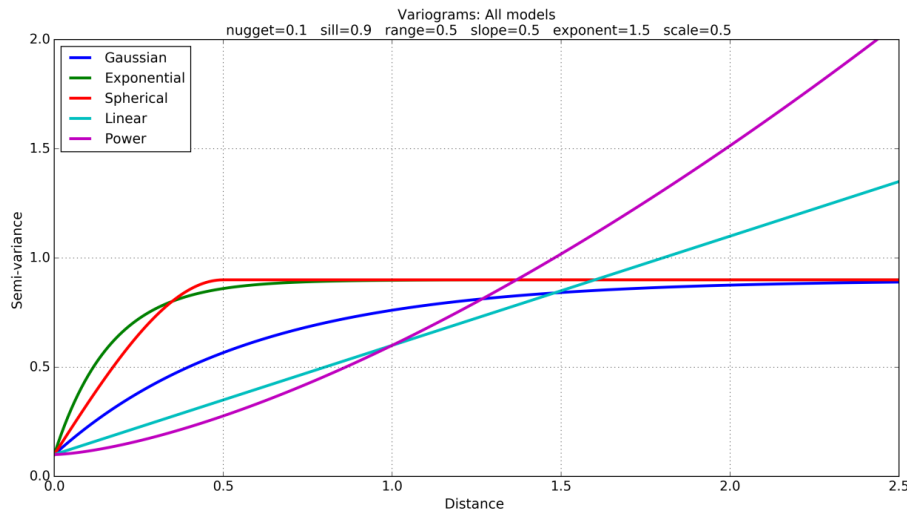
Fig. 2 Examples of variogram models: Gaussian (blue), Exponential (green), Spherical (red), Linear (cyan) and Power (magenta). Used parameters are shown at the top of the figure. The horizontal axis represents the independent variable h and the vertical axis the γ value used in formulas (12)-(16).

3.3.3 The Universal Kriging

The geostatistics method known as *universal Kriging* (or *Kriging with a drift*) (Olea 1974; Kitanidis 1997) is based on the assumption that the measured geophysical field displays a large-scale spatial variability that can be represented as a *deterministic* function, and a small-scale spatial variability, the *stochastic* part, involving spatial correlations inferable from the variogram. Then:

$$z(\boldsymbol{x}) = m(\boldsymbol{x}) + \epsilon(\boldsymbol{x}), \tag{17}$$

where $m(\boldsymbol{x})$, called the *drift*, represents the deterministic part of $z(\boldsymbol{x})$, while the function $\epsilon(\boldsymbol{x})$ represents the stochastic part of $z(\boldsymbol{x})$ with zero mean ($E[\epsilon(\boldsymbol{x})] = 0$) and a definite correlation structure described by its covariance R (linked to the semivariance by Eq. (11)). The ordinary Kriging method is based on assumption that m is a constant without any spatial characterization, and the spatial description is left only to the stochastic part $\epsilon(\boldsymbol{x})$. The universal Kriging method, however, requires an a priori knowledge of the geophysical quantity to be described, which is used in the characterization of the deterministic part. For example, *fo*F2, on average, is characterized by spatial gradients that are bigger at mid-low latitudes than at mid-high latitudes, and the same spatial gradient features will be embedded in the IG_{12} activity index. Using the universal Kriging method, this large-scale deterministic behavior can be included in the drift part, which allows to characterize also regions distant from assimilated points, without the need to employ non-stationary variogram models.

The drift part can be represented by (Kitanidis 1997):

$$m(\boldsymbol{x}) = \sum_{k=1}^{p} f_k(\boldsymbol{x})\beta_k, \tag{18}$$

where $f_1(\boldsymbol{x}), \ldots, f_p(\boldsymbol{x})$ are known functions of spatial coordinates $\boldsymbol{x}$ and are called *base functions*, and $\beta_1, \ldots, \beta_p$ are unknown deterministic coefficients referred to as *drift coefficients*. In our case, $m(x,y) = A + Bx + Cy$, namely, the deterministic part is a two-dimensional *regional linear mean* in the x (longitude) and y (latitude) variables.

Hence, the spatial function is given by:

$$z(\boldsymbol{x}) = \sum_{k=1}^{p} f_k(\boldsymbol{x})\beta_k + \epsilon(\boldsymbol{x}). \tag{19}$$

Thus, the goal is to use Eq. (9) to derive an estimate of z at $\boldsymbol{x}_0$, from measurements $z(\boldsymbol{x}_1), \ldots, z(\boldsymbol{x}_n)$, with the assumption that Eq. (19) follows the unbiasedness and minimum variance conditions.

The unbiasedness condition, using Eq. (9), may be written:

$$E[\hat{z}(\boldsymbol{x_0}) - z(\boldsymbol{x_0})] = E\left[\sum_{i=1}^{n} \lambda_i z(\boldsymbol{x_i}) - z(\boldsymbol{x_0})\right] = 0, \tag{20}$$

making use of Eqs (18)-(19) we get (remembering that $E[\epsilon(\boldsymbol{x})] = 0$) (Kitanidis 1997):

$$\sum_{k=1}^{p}\left(\sum_{i=1}^{n} \lambda_i f_k(\boldsymbol{x_i}) - f_k(\boldsymbol{x_0})\right)\beta_k = 0. \tag{21}$$

For this condition to hold for any values of $\beta_1, \dots, \beta_p$ it is required that:

$$\sum_{i=1}^{n} \lambda_i f_k(\boldsymbol{x_i}) = f_k(\boldsymbol{x_0}) \qquad k = 1, \dots \dots, p. \tag{22}$$

This set of p constraints must be satisfied by the λ coefficients, and each unbiasedness condition has the effect of eliminating an unknown drift coefficient.

The variance of the estimation error, making use of the unbiasedness condition, involves only the stochastic part $\epsilon(\boldsymbol{x})$, which we assume described by its covariance $R(\boldsymbol{x}, \boldsymbol{x}')$, leading to (Kitanidis 1997):

$$\begin{aligned}
E\left[(\hat{z}(\boldsymbol{x_0}) - z(\boldsymbol{x_0}))^2\right] &= E\left[\left(\sum_{i=1}^{n} \lambda_i \epsilon(\boldsymbol{x_i}) - \epsilon(\boldsymbol{x_0})\right)^2\right] \\
&= \sum_{i=1}^{n}\sum_{j=1}^{n} \lambda_i \lambda_j R(\boldsymbol{x_i}, \boldsymbol{x_j}) - 2\sum_{i=1}^{n} \lambda_i R(\boldsymbol{x_i}, \boldsymbol{x_0}) + R(\boldsymbol{x_0}, \boldsymbol{x_0}).
\end{aligned} \tag{23}$$

Thus, coefficients $\lambda_1, \dots, \lambda_n$ will be estimated by minimizing the expression in Eq. (23), which in turn depends on the p linear constraints of the unbiasedness condition Eq.(22). The minimum variance condition make the Kriging method an optimization problem, with assigned constraints, that can be resolved by means of *Lagrangian multiplier method,* which has the general form:

$$min \, f(\lambda_1, \dots, \lambda_n), \tag{24a}$$

$$g_k(\lambda_1, \dots, \lambda_n) = b_k \quad k = 1, \dots, p. \tag{24b}$$

In our case:

$$f(\lambda_1, \dots, \lambda_n) = \sum_{i=1}^{n}\sum_{j=1}^{n} \lambda_i \lambda_j R(\boldsymbol{x_i}, \boldsymbol{x_j}) - 2\sum_{i=1}^{n} \lambda_i R(\boldsymbol{x_i}, \boldsymbol{x_0}) + R(\boldsymbol{x_0}, \boldsymbol{x_0}), \tag{24c}$$

$$g_k(\lambda_1, \dots, \lambda_n) = \sum_{i=1}^{n} \lambda_i f_k(\boldsymbol{x_i}), \tag{24d}$$

$$b_k = f_k(\boldsymbol{x_0}). \tag{24e}$$

The *Lagrangian* (*L*) is:

$$L(\lambda_1, \ldots, \lambda_n, v_1, \ldots, v_p)$$
$$= f(\lambda_1, \ldots, \lambda_n) + 2v_1(g_1(\lambda_1, \ldots, \lambda_n) - b_1) + \cdots + 2v_p(g_p(\lambda_1, \ldots, \lambda_n) - b_p), \quad \text{(24f)}$$

where $v_1, \ldots, v_p$ are parameters called *Lagrange multipliers,* and number 2 is used only for convenience.

By taking derivatives of *L* with respect to $\lambda_1, \ldots, \lambda_n$ and setting them to zero

$$\frac{\partial f}{\partial \lambda_i} + 2v_i \frac{\partial g_i}{\partial \lambda_i} + \cdots + 2v_p \frac{\partial g_p}{\partial \lambda_i} = 0 \quad i = 1, \ldots, n, \quad \text{(24g)}$$

we obtain

$$\sum_{j=1}^{n} R(x_i, x_j)\lambda_j + \sum_{k=1}^{p} f_k(x_i)v_k = R(x_i, x_0) \quad i = 1, \ldots, n. \quad \text{(25)}$$

Eqs (22) and (25) form the Kriging system which consists of $n + p$ linear equations with $n + p$ unknowns which can be easily resolved.

The Kriging system can be put also in a matrix notation. Let x be the vector of unknowns:

$$x = \begin{pmatrix} \lambda_1 \\ \ldots \\ \lambda_n \\ v_1 \\ \ldots \\ v_p \end{pmatrix}, \quad \text{(26a)}$$

b the right-hand side vector:

$$b = \begin{pmatrix} R(x_1, x_0) \\ \ldots \\ R(x_n, x_0) \end{pmatrix}, \quad \text{(26b)}$$

and A the matrix of coefficients:

$$A = \begin{pmatrix} R(x_1, x_1) & R(x_1, x_2) & \ldots & R(x_1, x_n) & f_1(x_1) & f_2(x_1) & \ldots & f_p(x_1) \\ R(x_2, x_1) & R(x_2, x_2) & \ldots & R(x_2, x_n) & f_1(x_2) & f_2(x_2) & \ldots & f_p(x_2) \\ \ldots & \ldots & \ldots & \ldots & \ldots & \ldots & \ldots & \ldots \\ R(x_n, x_1) & R(x_n, x_2) & \ldots & R(x_n, x_n) & f_1(x_n) & f_2(x_n) & \ldots & f_p(x_n) \end{pmatrix}. \quad \text{(26c)}$$

Hence, the Kriging system can be written as:

$$Ax = b. \quad \text{(26d)}$$

3.4 Comparison of IRI UP and IRTAM methodology

Both IRI UP and IRTAM belong to a class of assimilative models that use the underlying empirical quiet-time IRI representation of the ionosphere to constrain the process of its elastic transformation into a better match with observations. The final product of both models, an updated 2D map of *fo*F2, hmF2, B0 (or any other characteristic in IRI) follows the ionospheric variability much closer than the background IRI climatological model. Such updates can be made every time a new measurement is available, typically at 15 minute cadence,

and feature a spatial super-resolution capability that modern ionosonde networks can now afford in Europe and the world at large. The underlying IRI representation ensures that, when and where measurements are not available, the assimilative model keeps its updates compatible with the empirical knowledge of the system: models gracefully retreat to the quiet-time ionosphere outside the sensor coverage areas.

Both models preserve the spatial/diurnal expansion basis of the IRI formalism and manipulate other model constituents into agreement with available measurements. Manipulation techniques, however, are significantly different for IRI UP and IRTAM. While IRI UP adjusts, at local points, the "solar activity" driver of the IRI model to compensate observed deviations between modelled and measured values, IRTAM uses a 24-hour window of deviations to adjust original coefficients of the diurnal/spatial IRI expansion. The models use different concepts to fill gaps caused by the limited availability of measurements: IRI UP interpolates missing values of the effective activity index using an optimally selected variogram, and IRTAM builds interpolated maps of deviations themselves, individually for different diurnal harmonics, assuming that slower changing "eigen" modes of the diurnal ionospheric dynamics are applicable at larger distances away from sensor sites.

Different strategies of protecting the assimilation from the measurement noise caused by occasional ionogram autoscaling mistakes are adopted by two models. IRTAM uses a low-pass temporal filter as a part of its diurnal harmonics analysis to smooth out data jitter, outliers, and low-confidence values; IRI UP discards computations that result in unreasonable $IG_{12\mathrm{eff}}$ and $R_{12\mathrm{eff}}$ maps. Further investigation is warranted to study the intriguing capability of both models to predict, spatially and temporally, the ionospheric variability during periods of increased geomagnetic activity, as well as their capability to withstand input data noise for real-time applications.

4 Results and discussion

4.1 Variogram statistics

For every hour of the studied period (9 March 2015 0 UT - 25 March 2015 23 UT), foF2 and M(3000)F2 values are assimilated from stations listed in Table 1 to calculate punctual $IG_{12\mathrm{eff}}$ and $R_{12\mathrm{eff}}$ values. Then, the Universal Kriging method is used to interpolate these values over the chosen grid (15°W÷45°E in longitude, 30°N÷60°N in latitude, with a 0.1°x0.1° resolution) using any of the five variogram models previously described, in order to evaluate which of these gives the best results against foF2 and M(3000)F2 values recorded at the test stations. An example of $IG_{12\mathrm{eff}}$ and $R_{12\mathrm{eff}}$ maps are shown in Fig. 3. $IG_{12\mathrm{eff}}$ and $R_{12\mathrm{eff}}$ values are then extracted from these maps for Fairford and San Vito grid-points and given as input to the IRI model, obtaining updated foF2 and M(3000)F2 values (and so hmF2 and foE updated values). These updated values are then compared with those measured at the test stations through the following statistical quantities (Root Mean Square Error ($RMSE$), Normalized Root Mean Square Error ($NRMSE$), Pearson correlation coefficient ρ, Mean delta, Standard Deviation delta):

$$RMSE \ = \ \sqrt{\frac{\sum_{i=1}^{N}\left(X_{\mathrm{calculated},i} - X_{\mathrm{ionosonde},i}\right)^{2}}{N}}, \tag{27}$$

where X stands for foF2 or M(3000)F2, the subscript *calculated* refers to updated values while the subscript *ionosonde* refers to values recorded by the ionosonde (the index i runs on the N hourly values of the time series);

$$NRMSE \ = \ \frac{RMSE(X_{\mathrm{calculated}}, X_{\mathrm{ionosonde}})}{\overline{X}_{\mathrm{ionosonde}}} \cdot 100, \tag{28}$$

where $\overline{X_{\text{ionosonde}}}$ is the arithmetic mean over time of $X_{\text{ionosonde}}$;

$$\rho = \frac{cov(X_{\text{calculated}}, X_{\text{ionosonde}})}{\sigma_{X_{\text{calculated}}} \sigma_{X_{\text{ionosonde}}}} \in [-1,1], \tag{29}$$

where cov is the covariance and σ the standard deviation;

$$Mean\ delta = \frac{\sum_{i=1}^{N}(X_{\text{calculated},i} - X_{\text{ionosonde},i})}{N}, \tag{30}$$

$$Standard\ Deviation\ delta =$$
$$\sqrt{\frac{\sum_{i=1}^{N}\left[(X_{\text{calculated},i} - X_{\text{ionosonde},i}) - Mean\ delta\ (X_{\text{calculated}} - X_{\text{ionosonde}})\right]^2}{N}}. \tag{31}$$

In addition, also the following percentage of discarded points is calculated:

$$\%\ discarded = \frac{\#\ total\ maps - \#\ good\ maps}{\#\ total\ maps}, \tag{32}$$

where $\#\ good\ maps$ is the cumulative number of $IG_{12\text{eff}}$ or $R_{12\text{eff}}$ maps which have passed some tests and $\#\ total\ maps$ is the total potential number of maps. Thus, $\%\ discarded$ gives the percentage of maps not produced by the method, since the number of assimilated stations was lower than four, plus those produced by the method but the use of which might lead to errors. For instance, there are cases for which semivariance values represented in the experimental variogram are so scattered and randomly distributed that cannot be fitted by any of the five variogram model functions with an acceptable degree of confidence, or cases for which the fitting function is an approximately straight horizontal line independently of the used model. These variograms lead to unrealistical $IG_{12\text{eff}}$ and $R_{12\text{eff}}$ maps that should be discarded. A decision was made to discard variograms (and consequently the corresponding maps) for which both the fitting procedure failed and the exponent *s* for the power model (Eq. (15)) is less than 0.1, i.e. it tends to a nearly horizontal straight line. In Table 2-3 statistical parameters (27)-(32) are calculated for Fairford and San Vito ionospheric stations, for all five variogram methods used, for *fo*F2 and *M*(3000)F2 respectively. In Table 4 the same statistical parameters are calculated for *hm*F2 using the spherical model for $IG_{12\text{eff}}$ and the linear model for $R_{12\text{eff}}$.

Table 2 Statistical results, for both test stations, Fairford and San Vito, for *fo*F2 using all five variogram models.

Station	Ionospheric characteristic	Variogram method	RMSE [MHz]	NRMSE [%]	Correlation Coefficient	Mean delta [MHz]	Standard Deviation delta [MHz]	discarded %
Fairford	foF2	linear	0.26	3.97	0.99	0.04	0.27	6.37
		power	0.26	3.92	0.99	0.03	0.27	6.37
		gaussian	0.27	4.12	0.99	0.02	0.28	6.37
		spherical	0.26	3.90	0.99	0.02	0.27	6.37
		exponential	0.26	3.93	0.99	0.02	0.27	6.37
San Vito	foF2	linear	0.38	5.17	0.99	-0.08	0.39	6.37
		power	0.39	5.27	0.99	-0.09	0.40	6.37

		gaussian	0.37	5.00	0.99	-0.07	0.38	6.37
		spherical	0.37	5.02	0.99	-0.08	0.38	6.37
		exponential	0.37	5.03	0.99	-0.08	0.38	6.37

Table 3 Same as Table 2, for $M(3000)F2$.

Station	Ionospheric characteristic	Variogram method	RMSE	NRMSE %	Correlation Coefficient	Mean delta	Standard Deviation delta	discarded %
Fairford	M(3000)F2	linear	0.081	2.64	0.92	0.006	0.093	23.77
		power	0.082	2.68	0.93	0.007	0.095	23.77
		gaussian	0.086	2.81	0.92	0.010	0.099	23.77
		spherical	0.084	2.75	0.93	0.012	0.097	23.77
		exponential	0.083	2.72	0.93	0.011	0.095	23.77
San Vito	M(3000)F2	linear	0.098	3.18	0.89	0.051	0.102	23.77
		power	0.101	3.28	0.88	0.054	0.104	23.77
		gaussian	0.108	3.48	0.87	0.058	0.110	23.77
		spherical	0.103	3.35	0.88	0.056	0.106	23.77
		exponential	0.102	3.30	0.88	0.054	0.104	23.77

Table 4 Same as Table 2, for $hmF2$ using the spherical model for $IG_{12\text{eff}}$ and the linear model for $R_{12\text{eff}}$.

Station	Ionospheric characteristic	Variogram method	RMSE [km]	NRMSE %	Correlation Coefficient	Mean delta [km]	Standard Deviation delta [km]	discarded %
Fairford	hmF2	IG12eff = spherical R12eff = linear	11.57	3.96	0.94	-0.44	13.78	28.68
San Vito	hmF2	IG12eff = spherical R12eff = linear	13.57	4.63	0.92	-5.34	15.44	28.68

Table 2-3 highlights that, for foF2 and $M(3000)$F2, all five methods show little differences. A close inspection of results of Table 2-3 leads however to the choice of the spherical model for foF2 and the linear model for $M(3000)$F2 as the best variograms. Thus, using the spherical method to obtain $IG_{12\text{eff}}$ maps, with which we get updated foF2 values, and the linear method to obtain $R_{12\text{eff}}$ maps, with which we get updated $M(3000)$F2 values, updated hmF2 values are obtained. $R_{12\text{eff}}$ values are used also to update foE values, that are used in the hmF2 calculation. As explained in the previous section, each variogram model displays its own small-scale and large-scale behavior to which are linked some mathematical implications, which imply the choice of the proper experimental variogram fitting procedure. However, a thorough knowledge of the geophysical quantities that have to be interpolated can help in the variogram model choice. For example, the electron density spatial distribution at mid latitudes shows, on average, spatial gradients with a very large scale, ranging from higher values at mid-low latitudes to lower values at mid-high latitudes. With the use of the universal Kriging method this large-scale spatial component can be represented by the regional linear mean described by the drift coefficients of Eq. (18). This is why for foF2 the spherical variogram model was chosen. For a more spatially variable characteristics like $M(3000)$F2, things become harder. In this case, the choice of the best variogram model was guided by the overall statistical analysis of Table 3, without any a priori hypothesis. Hence, for $M(3000)$F2, by choosing the linear variogram model, the stochastic part contributes to the description of the $M(3000)$F2 large-scale spatial behavior.

The last column of Table 2-4 shows the percentage of discarded maps and then the percentage of missing updated values. This value is small for foF2 (6.37%) and becomes larger for $M(3000)$F2 (23.77%) and hmF2 (28.68%). The large value for hmF2 is simply due to the fact that it depends on both foF2 and $M(3000)$F2 values (Eq. (5a)). The difference between foF2 and $M(3000)$F2 percentages is instead more difficult to explain; the reason is likely due to the intrinsic different spatial behavior between these two ionospheric characteristics, which make the spatial description of $M(3000)$F2 more challenging.

4.2 IG_{12eff} and R_{12eff} indices

Figure 3 shows an example of IG_{12eff} and R_{12eff} maps for the 17 March 2015 (calendar day 76) at 11 UT, generated by using the spherical variogram model for IG_{12eff} and the linear variogram model for R_{12eff}. Both maps show important spatial gradients with very extended magnitude scales which reflect the assimilated spatial variability. It is worth noting that in Fig. 3 maxima and minima of IG_{12eff} and R_{12eff} are opposite; this is due to the fact that for that moment the highest values of foF2 and $M(3000)$F2 are recorded at Moscow and Warsaw, and the dependence between foF2 and IG_{12} is direct, while that between $M(3000)$F2 and R_{12} is inverse. Of course, to catch small-scale spatial structures, the ionospheric assimilated stations distribution is fundamental for two different reasons: 1) having many stations at very small distance allows to populate the part of the experimental variogram near the origin, which is essential to describe the small-scale spatial behavior of the represented characteristic; 2) to increase the goodness of the fitted variogram model. The large-scale spatial distribution of assimilated stations is particularly important to spread over the map the information embedded in the variogram (even though this need is highly decreased using the universal Kriging, whatever variogram model is used).

Two maps, as those shown in Fig. 3, are then used as input to the IRI model (point 5. of Section 2.3) to obtain updated values of foF2, $M(3000)$F2, foE and hmF2. Figure 4 shows time series of IG_{12eff}, IG_{12}, R_{12eff} and R_{12}, for Fairford and San Vito, respectively, along with those of geomagnetic indices D_{st} and AE, which highlight the effects of the St. Patrick storm. The figure clearly shows that effective indices IG_{12eff} and R_{12eff} describe short-temporal variations, both for quiet and disturbed conditions. The power of the method is however mainly evident in the main and recovery phases of the storm. In particular, the IG_{12eff} time series correlates well with the D_{st} index, a sign that foF2 values, from which it derives, are significantly affected by storm induced effects; also oscillations in the recovery phase, seen especially in Fairford, tell us that also sub-storm induced effects are well described by this effective index. The pattern of variability shown by the R_{12eff} time series is more irregular than that of IG_{12eff}, highlighting however a more definite variability during the main phase of the storm.
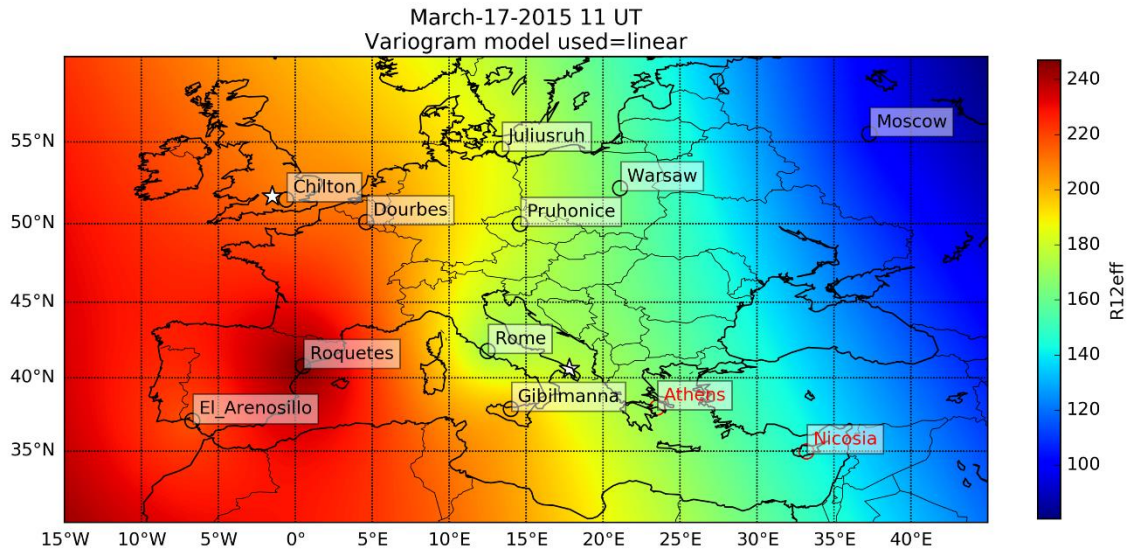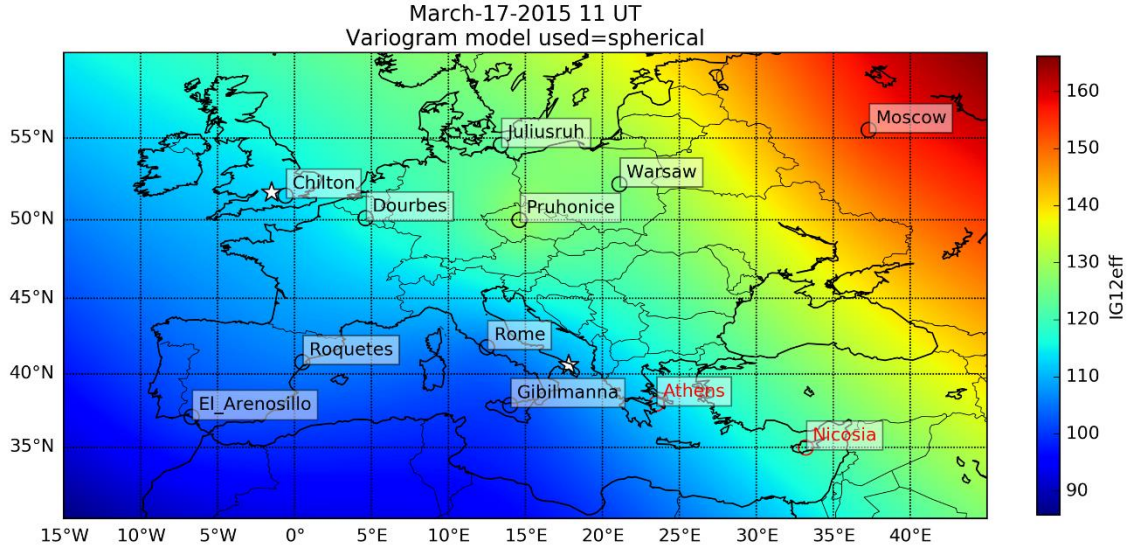
Fig. 3 (top panel) $IG_{12\text{eff}}$ and (bottom panel) $R_{12\text{eff}}$ maps for the 17 March 2015 (day 76) at 11 UT. They were generated by using the spherical variogram model for $IG_{12\text{eff}}$ and the linear variogram model for $R_{12\text{eff}}$. Black circles highlight the assimilated stations, red circles highlight stations, included in the stations list, for which values were not available. The two white stars mark the position of the two test stations, Fairford in the upper left corner and San Vito in the middle lower part of both panels.
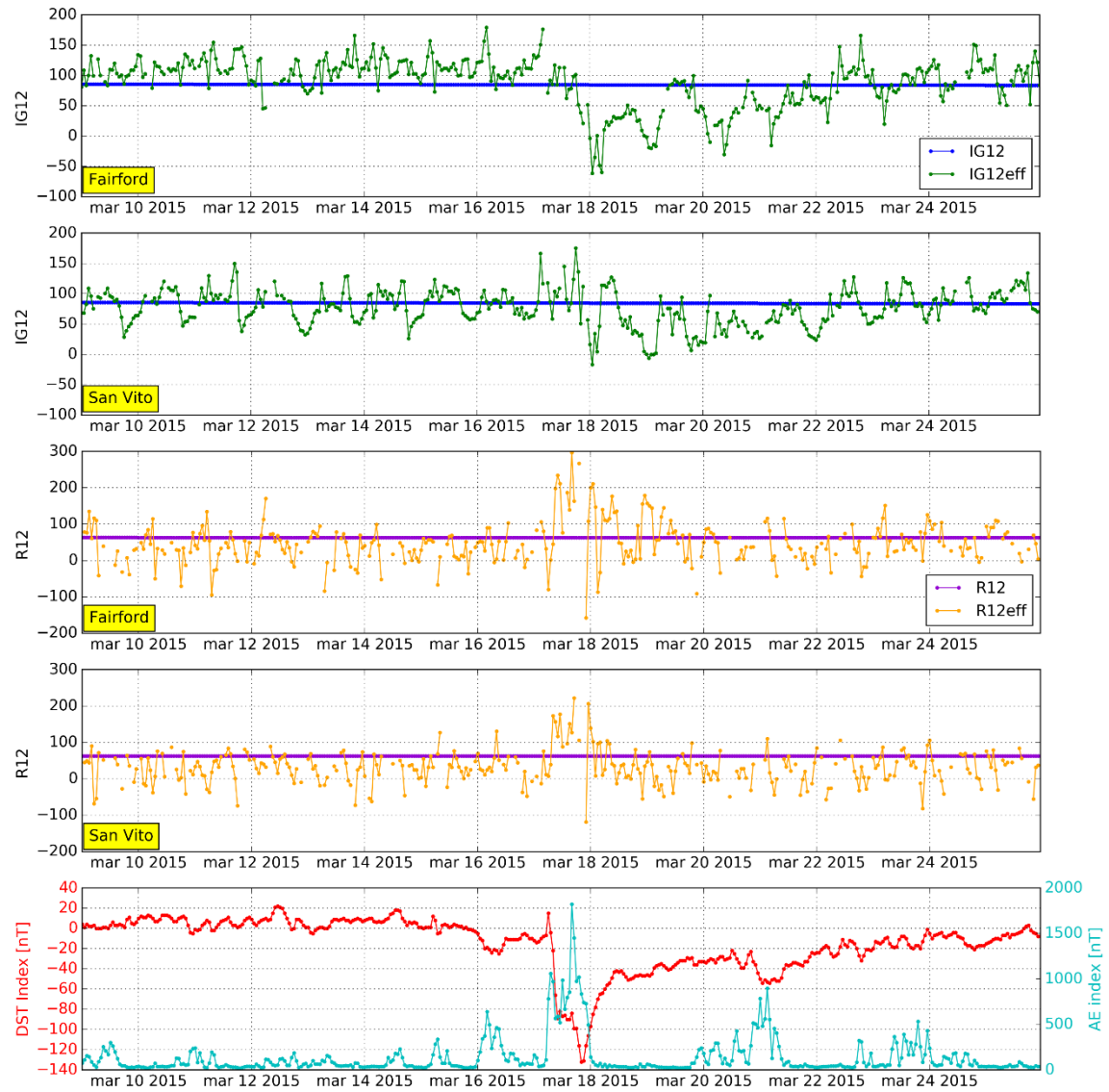
Fig. 4 From top to bottom, for the studied period, time series of: IG_{12} (blue) and $IG_{12\text{eff}}$ (green), for Fairford and San Vito; R_{12} (violet) and $R_{12\text{eff}}$ (orange), for Fairford and San Vito; D_{st} (red) and AE (cyan) magnetic indices.

4.3 Comparison with IRI and IRTAM models

Each method that, through data assimilation processes, has the purpose of improving an underlying model, needs to be compared, first of all, with the underlying model itself, and, when possible, with a model characterized by the same goal but based on different mathematical techniques. Hence, IRI UP will be compared first with IRI, while the second task will be accomplished by considering the IRTAM model (http://giro.uml.edu/IRTAM/, publicly available at http://giro.uml.edu/GAMBIT/) developed by Galkin et al. (2012). IRTAM assimilates data from the Global Ionospheric Radio Observatory (GIRO) (Reinisch and Galkin 2011) to update the climatological IRI background in terms of *fo*F2 and *hm*F2. The IRTAM model is global by design, i.e., it gives preference to smooth rather than detailed spatial representation, but, given that in the European sector it assimilates data from the same ionospheric stations considered by the method here proposed, it seems appropriate to perform a comparison between the two. Notably, the publicly available version of IRTAM does not treat Fairford and San Vito as control sites during its assimilation, but instead excludes nearby

Chilton (66 km away) and Rome (460 km) locations where older digisondes operate. This means that IRI UP is disadvantaged in this comparison as it does not assimilate the control sites and exercises its spatial prediction capability.

4.3.1 *fo*F2 statistical comparison

Figure 5a, for the quiet period from 9 March 2015 to 16 March 2015, and Fig. 5b, for the disturbed period from 17 March 2015 to 25 March 2015, show a comparison between *fo*F2 values autoscaled at Fairford and San Vito, and calculated by IRI (with the storm option on), by IRI UP and by IRTAM. Same figures show also the time series of the difference between values recorded by the ionosonde and those calculated by models. Statistical quantities (27)-(32) related to these time series are shown in Table 5. Figure 6 shows the histograms of differences between *fo*F2 values measured at Fairford and San Vito, and calculated by IRI, IRI UP, and IRTAM.
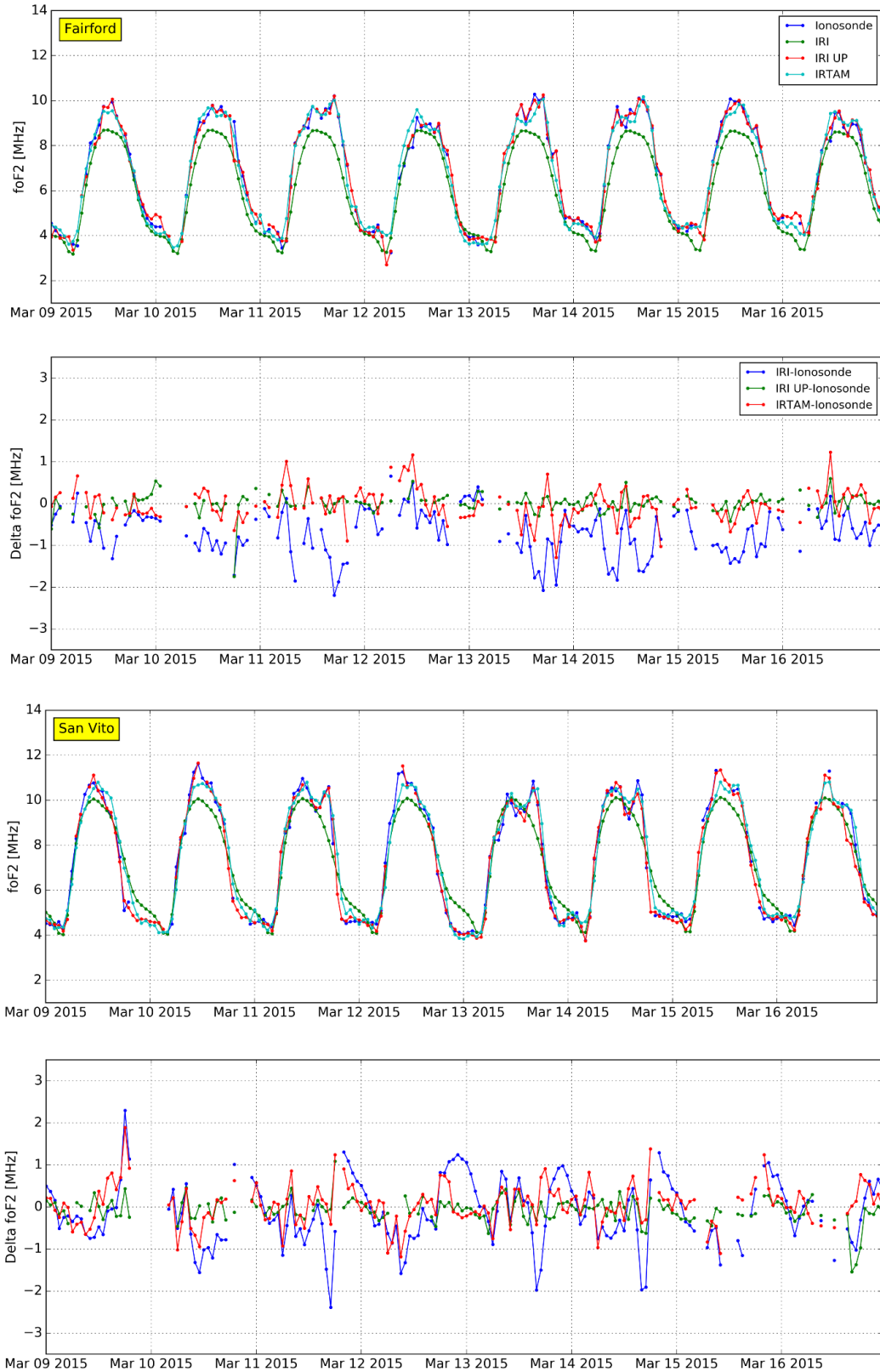
Fig. 5a Comparison between *fo*F2 values (blue) as measured by the ionosonde, and calculated by IRI (green) IRI UP (red), and IRTAM (cyan), for (first panel from the top) Fairford and (third panel from the top) San Vito, for the period from 9 March 2015 to 16 March 2015. Corresponding differences between measured and modelled values are also reported for Fairford (second panel from the top) and San Vito (fourth panel from the top).
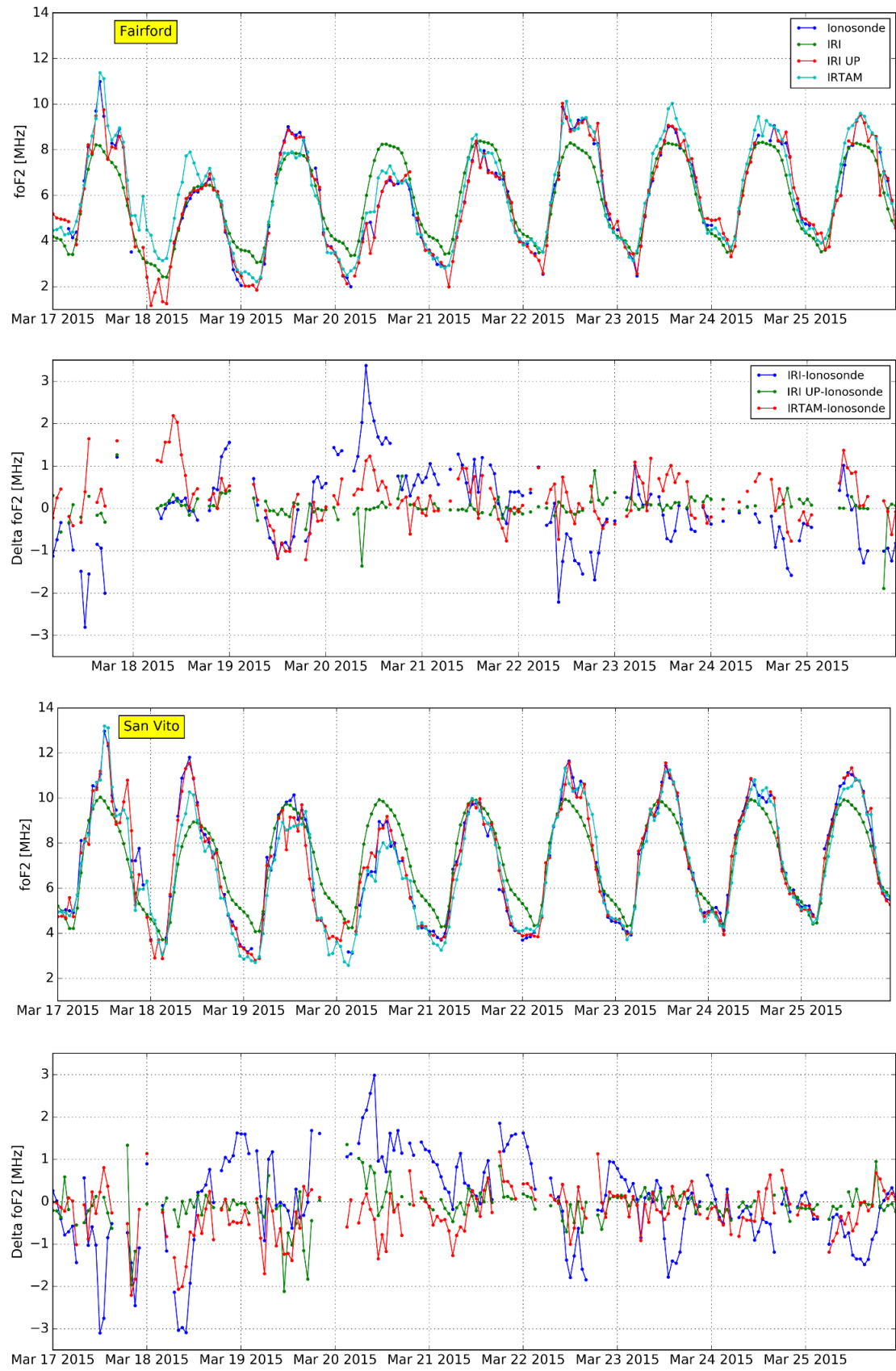
Fig. 5b Same as Fig. 5a but from 17 March 2015 to 25 March 2015.
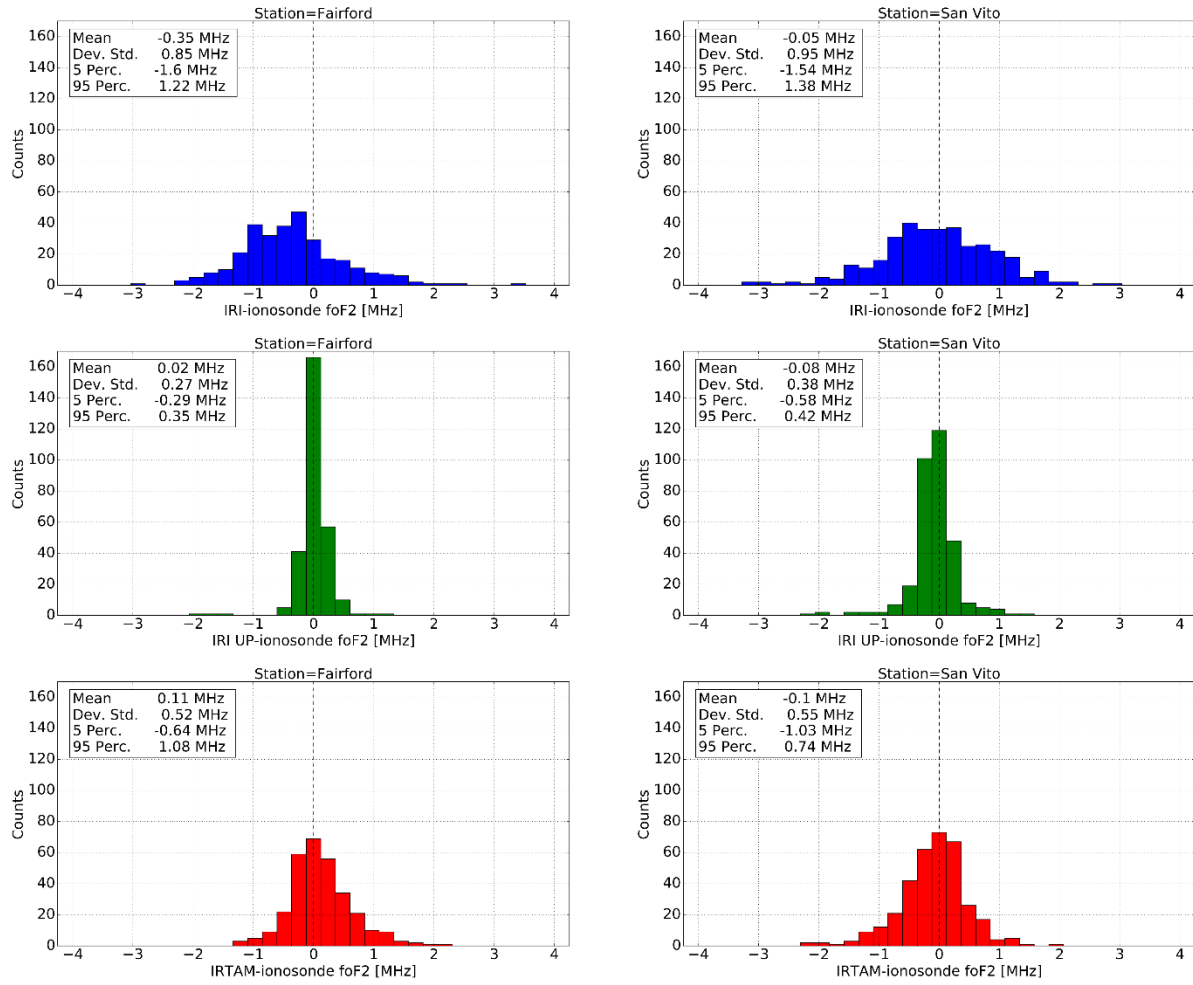
Fig. 6 Histograms of differences between measured *fo*F2 and calculated by IRI (blue), IRI UP (green), and IRTAM (red), for Fairford (left side) and San Vito (right side). In the upper left corner of each histogram the distribution mean, the standard deviation, the 5th and 95th percentiles are reported. The number of points in IRI and IRTAM histograms are the same (408), while those for IRI UP are slightly lower (382), taking into account the discarded maps (whose percentage is highlighted by the rightmost columns of Table 2).
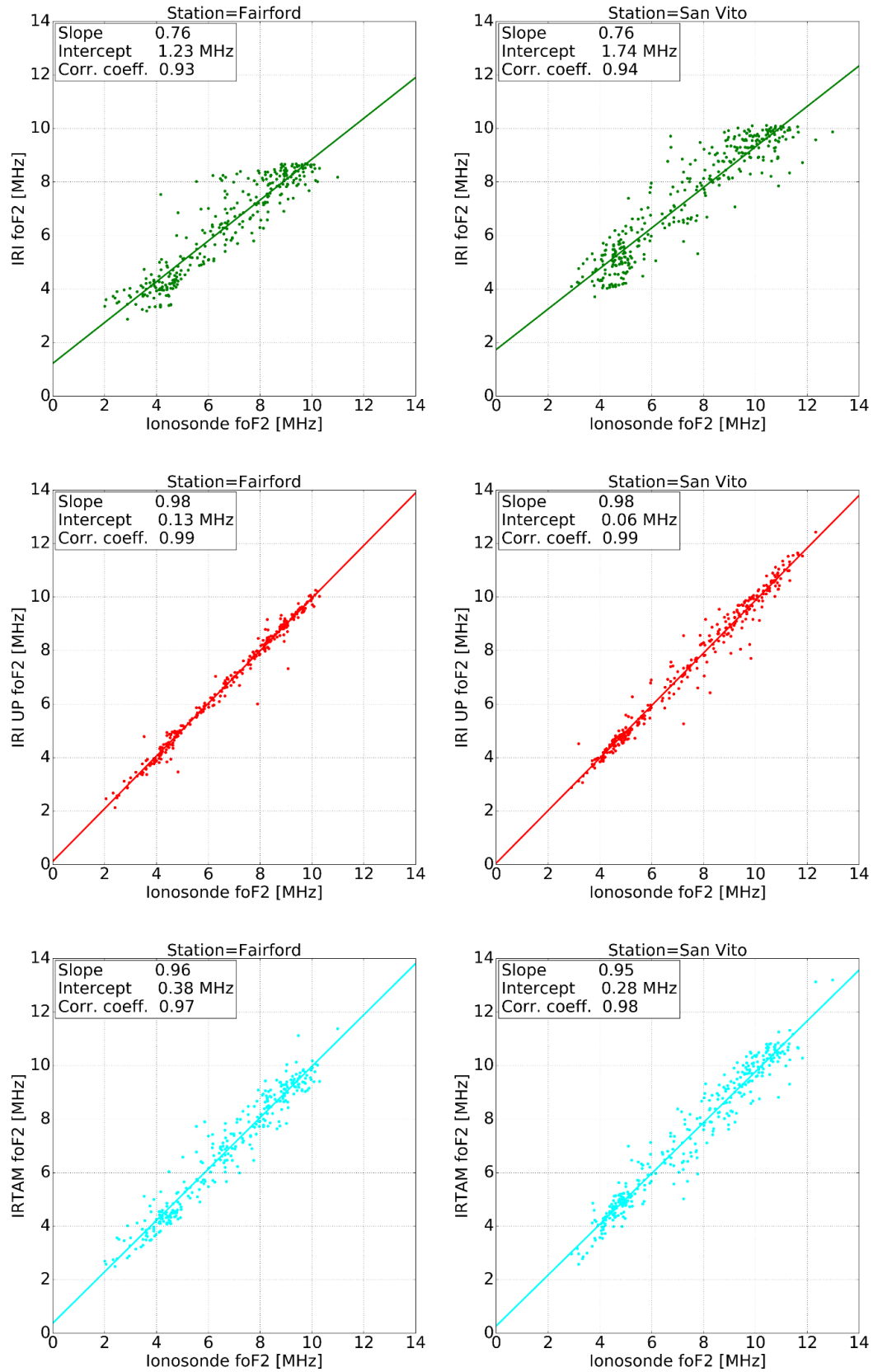
Fig. 7 Scatter plots of *fo*F2 values as measured by the ionosonde against ones modelled by IRI (green) , IRI UP (red), and IRTAM (cyan), for Fairford (left side) and San Vito (right side). In each plot the linear fit is drawn, with the corresponding slope and intercept shown in the upper left corner, where also the value of the Pearson's correlation coefficient is reported.

Figures 5a,b show that IRI performs: a) for quiet days, before the storm commencement and in the last part of the time window, a general underestimation of measured values at Fairford, while a more wavy behavior holds for San Vito; b) a general overestimation of measured values during the recovery phase of the storm; c) an important underestimation of measured values during the main phase of the storm (March 17-18). The relevant feature is however that the IRI storm option, for this particularly severe event, cannot properly describe the ionospheric plasma. On the other hand, IRI UP and IRTAM show, as expected, a better agreement with measured foF2 values. Specifically, the IRTAM model, although it is very efficient for quiet days, displays some deficiencies in the main phase of the storm. For example, at Fairford on March 18, IRTAM shows a general overestimation, while this does not happen for IRI UP. For the same period, IRTAM shows a general underestimation at San Vito, like IRI, but in a minor extent. This particular day (March 18), under severely disturbed conditions, demonstrates that, during the main phase of the storm, the ionosphere is really spatially variable, with very different foF2 values at Fairford and San Vito. This spatial variability is challenging for every model except IRI UP, whose behavior is good for both quiet and, more importantly, for disturbed conditions. This means that the spatial description of effective indices, made by the application of the universal Kriging spatial interpolation method, turns out to be very powerful for foF2, allowing to catch the different effects that the storm has at different latitudes. The latter statement is statistically supported by results shown in Table 5. Specifically, histograms shown in Fig. 6 point out that IRI UP performs better than IRI and IRTAM, with distributions that are more picked around the zero difference and with smaller dispersion values. Figure 6 shows that IRTAM has a good accuracy but less precision than IRI UP. The precision of each model can be verified visually in scatter plots of Fig. 7, which show that IRI and IRTAM values are more scattered than IRI UP ones. In conclusion, Figs. 5-7 and Table 5 tell us that, for foF2, the IRI UP model leads to a net improvement with respect to IRI and, to a minor extent, IRTAM.

4.3.2 hmF2 statistical comparison

An analogous comparison is made between measured hmF2 values at Fairford and San Vito and calculated by IRI, IRI UP, and IRTAM. Statistical quantities (27)-(32) related to these time series are shown in Table 6. Figure 8 shows histograms of differences between hmF2 values measured at Fairford and San Vito, and calculated by IRI, IRI UP, and IRTAM.
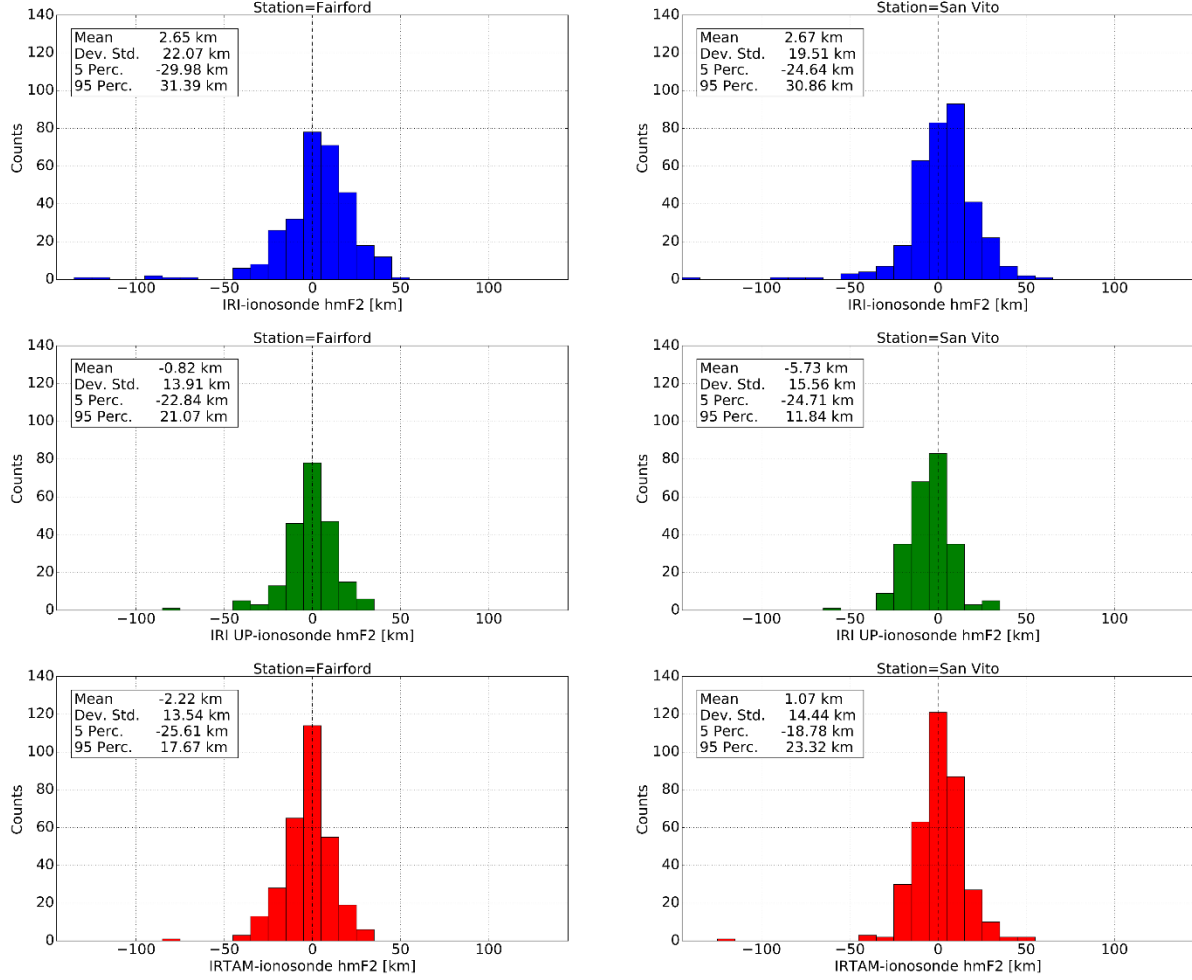
Fig. 8 Same as Fig. 6 but for *hm*F2. The number of points in IRI and IRTAM histograms are the same (408), while those for IRI UP are lower (291), taking into account the discarded maps (whose percentage is highlighted by the rightmost columns of Table 4).

Statistical quantities (27)-(32) of Table 6 show that IRI UP and IRTAM both improve the IRI output, but in this case values given as output by IRTAM are slightly better than IRI UP ones. These outcomes are supported also by statistical distributions of Fig. 8. However, in general, assimilation of measured ionospheric characteristics seems to be more effective to update *fo*F2 than *hm*F2. The reason of this is that *hm*F2 values, as described in Section 3.2, are not directly measured or inferred by the ionogram, but calculated by analytical formula. This mathematical passage, unavoidably, lowers the degree of precision of this characteristic. Furthermore, *hm*F2 isn't directly modeled by means of a single solar/ionospheric index, but it depends on both IG_{12} (through *fo*F2) and R_{12} (through $M(3000)$F2 and *fo*E); thus, errors related to the calculation of these indices can propagate and, normally, increase.

Table 5 Statistical results of the comparison between measured *fo*F2 and calculated by IRI, IRI UP, and IRTAM for both test stations.

| Station	Ionospheric characteristic	Comparison	RMSE [MHz]	NRMSE [%]	Correlation Coefficient	Mean delta [MHz]	Standard Deviation Delta [MHz]
Fairford	foF2	Ionosonde vs IRI	0.92	13.81	0.93	-0.35	0.85
		Ionosonde vs IRI UP	0.26	3.90	0.99	0.02	0.27
		Ionosonde vs IRTAM	0.53	8.07	0.97	0.11	0.52
San Vito	foF2	Ionosonde vs IRI	0.95	12.82	0.94	-0.05	0.95
		Ionosonde vs IRI UP	0.37	5.02	0.99	-0.08	0.38
		Ionosonde vs IRTAM	0.56	7.55	0.98	-0.10	0.55

Table 6 Same as Table 5, for *hm*F2.

| Station	Ionospheric characteristic	Comparison	RMSE [km]	NRMSE [%]	Correlation Coefficient	Mean delta [km]	Standard Deviation Delta [km]
Fairford	hmF2	Ionosonde vs IRI	22.23	7.61	0.84	2.65	22.07
		Ionosonde vs IRI UP	11.57	3.96	0.94	-0.44	13.78
		Ionosonde vs IRTAM	13.72	4.70	0.94	-2.22	13.54
San Vito	hmF2	Ionosonde vs IRI	19.69	6.72	0.86	2.67	19.51
		Ionosonde vs IRI UP	13.57	4.63	0.92	-5.34	15.44
		Ionosonde vs IRTAM	14.48	4.94	0.93	1.07	14.44

4.3.3 *fo*F2 and *hm*F2 example maps

Figures 9-11 are examples of *fo*F2 and *hm*F2 maps, for the chosen European grid, generated by IRI with the storm option off, IRI with the storm option on, and IRI UP, for three selected moments. Figure 9 represents a quiet moment on March 9 2015 (calendar day 68) at 15 UT, Fig. 10 and Fig. 11 disturbed moments on March 17 2015 (calendar day 76) at 11 UT and on March 18 2015 (calendar day 77) at 12 UT.

Figure 9 represents an afternoon snapshot of F2-layer characteristics, for quiet conditions. Quiet conditions represented by this figure are testified by the fact that IRI and IRI-STORM maps are identical, for both *fo*F2 and *hm*F2; those associated to IRI UP show instead slight differences for *fo*F2 and significant differences for *hm*F2. For *fo*F2, IRI UP preserves more or less the same gradient direction shown by IRI but with a sensible intensification in magnitude, clear in the upper right and lower left corners; furthermore, a slight increase of *fo*F2 values over Rome is evident, which is caused by an assimilation of an *fo*F2 value at the ionospheric station of Rome well above the monthly median value. On the contrary, the *hm*F2 IRI UP map shows an important decrease of values, well below monthly median ones, in the eastern part of the map, preserving however the gradient direction in the other parts of the map.
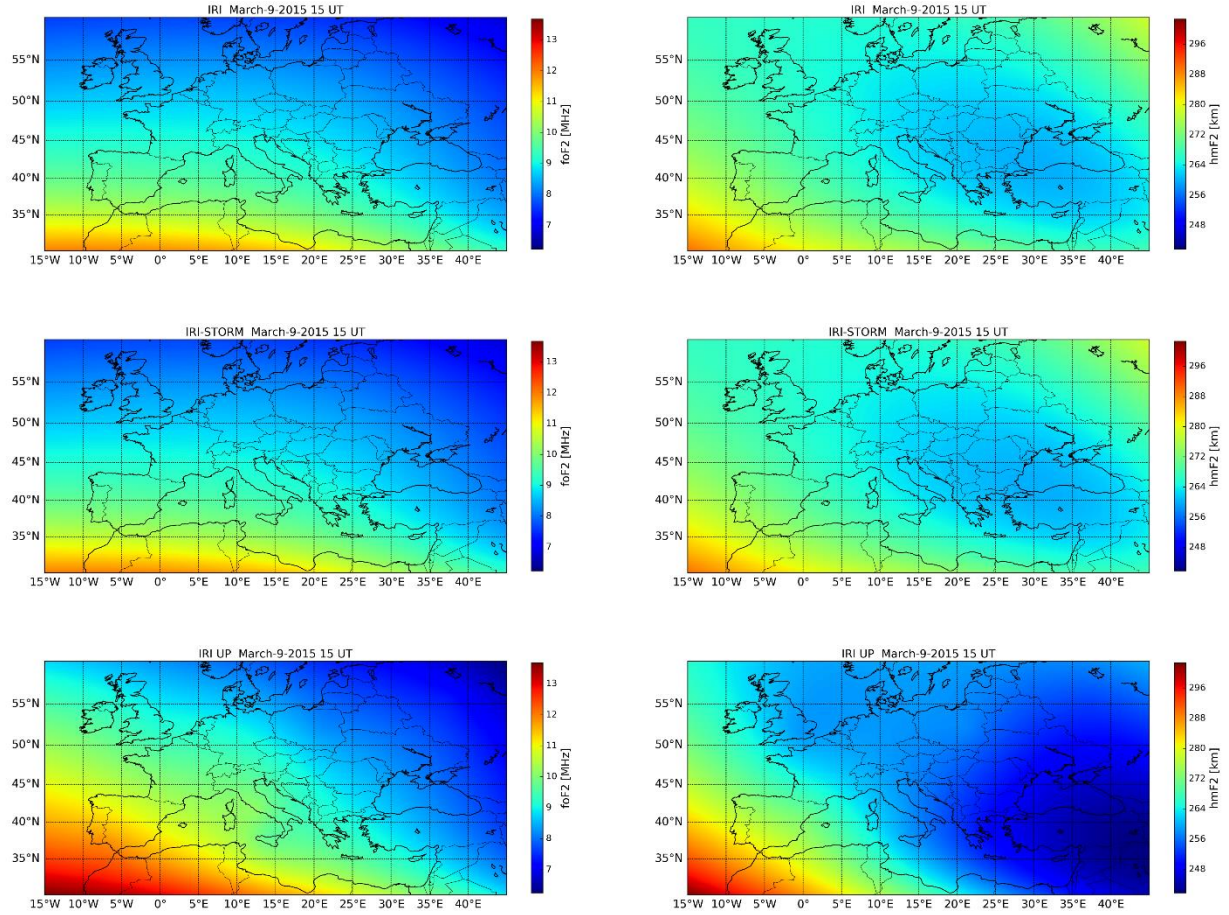
Fig. 9 Examples of maps for (left side) *fo*F2 and (right side) *hm*F2, generated by (top) IRI with the storm option off, (middle) IRI with the storm option on, and (bottom) IRI UP. They refer to the quiet day of March 9 2015 (calendar day 68) at 15 UT.

Figure 10 represents a near-noon snapshot of F2-layer characteristics, for disturbed conditions. Despite being a disturbed moment, IRI and IRI-STORM maps are identical, both for *fo*F2 and *hm*F2 since the storm option uses a weighted mean of a_p values for the previous 33 hours. Maps of Fig. 10 are calculated for a moment for which the storm has started only since a few hours (~6 h), and has not reached its maximum development (D_{st} index achieves its minimum on 17 March at 23 UT). The IRI storm option in the early phase of the storm cannot be effective in catching storm effects on the ionosphere. Instead, IRI UP maps turn out to be very effective, and their goodness is statistically supported by the analysis described in previous sections. These maps, obtained by means of updated effective indices, can properly represent both very fast ionospheric changes, from an hour to the next (and also every 15 minutes, it depends on the ionosonde sounding repetition rate), and also small spatial changes thanks to the universal Kriging interpolation method.
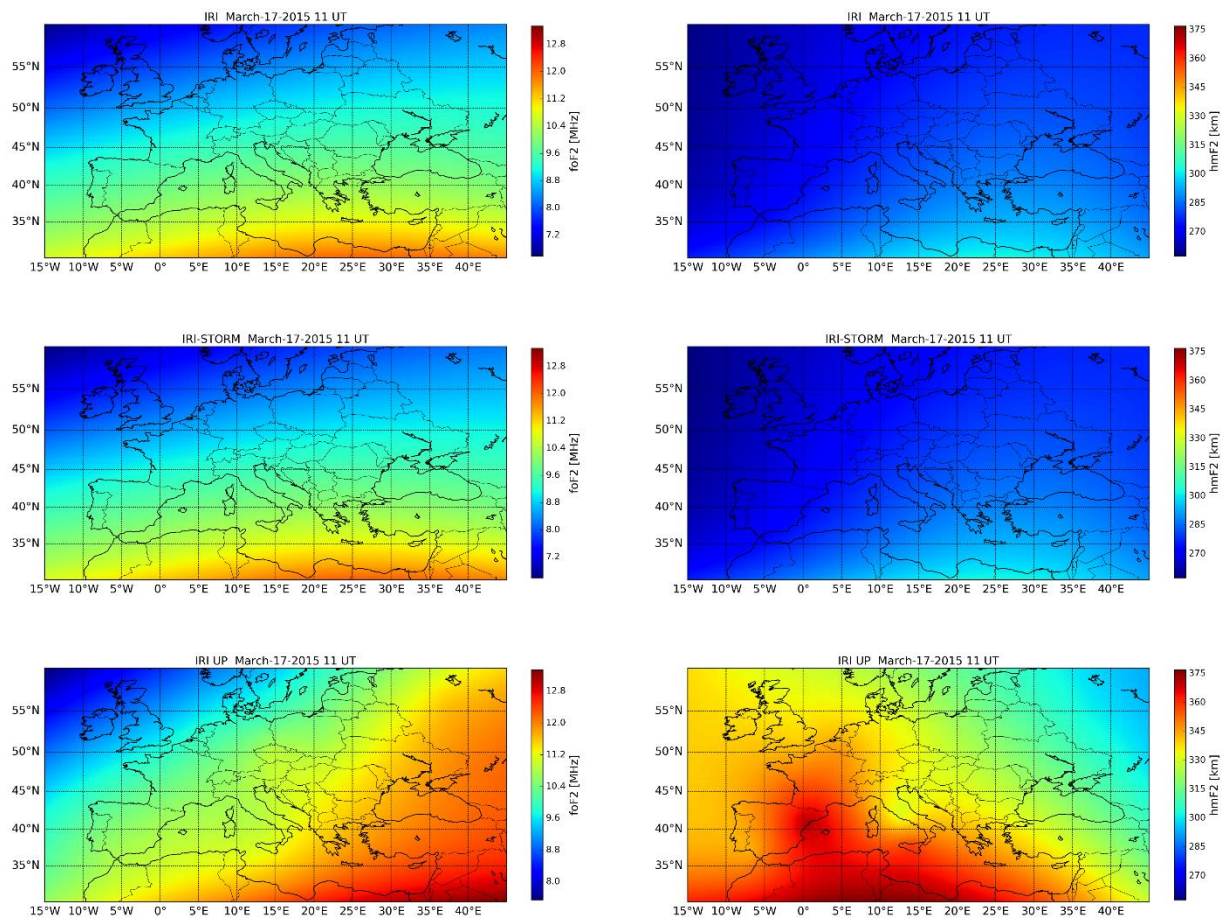
Fig. 10 Same as Fig. 9 but for the disturbed day March 17 2015 (calendar day 76) at 11 UT.

Figure 11 represents a noon snapshot of F2-layer characteristics, for very disturbed conditions. In this case, being the storm well developed, IRI and IRI-STORM maps show large differences in magnitude, for both *fo*F2 and *hm*F2, even though the gradient direction is similar. IRI UP map for *fo*F2 shows a gradient which is similar to that of IRI and IRI-STORM, although it manifests a wavier behavior than the more linear IRI ones. For *hm*F2 differences between IRI and IRI UP are again very important, both in gradient direction and magnitude.
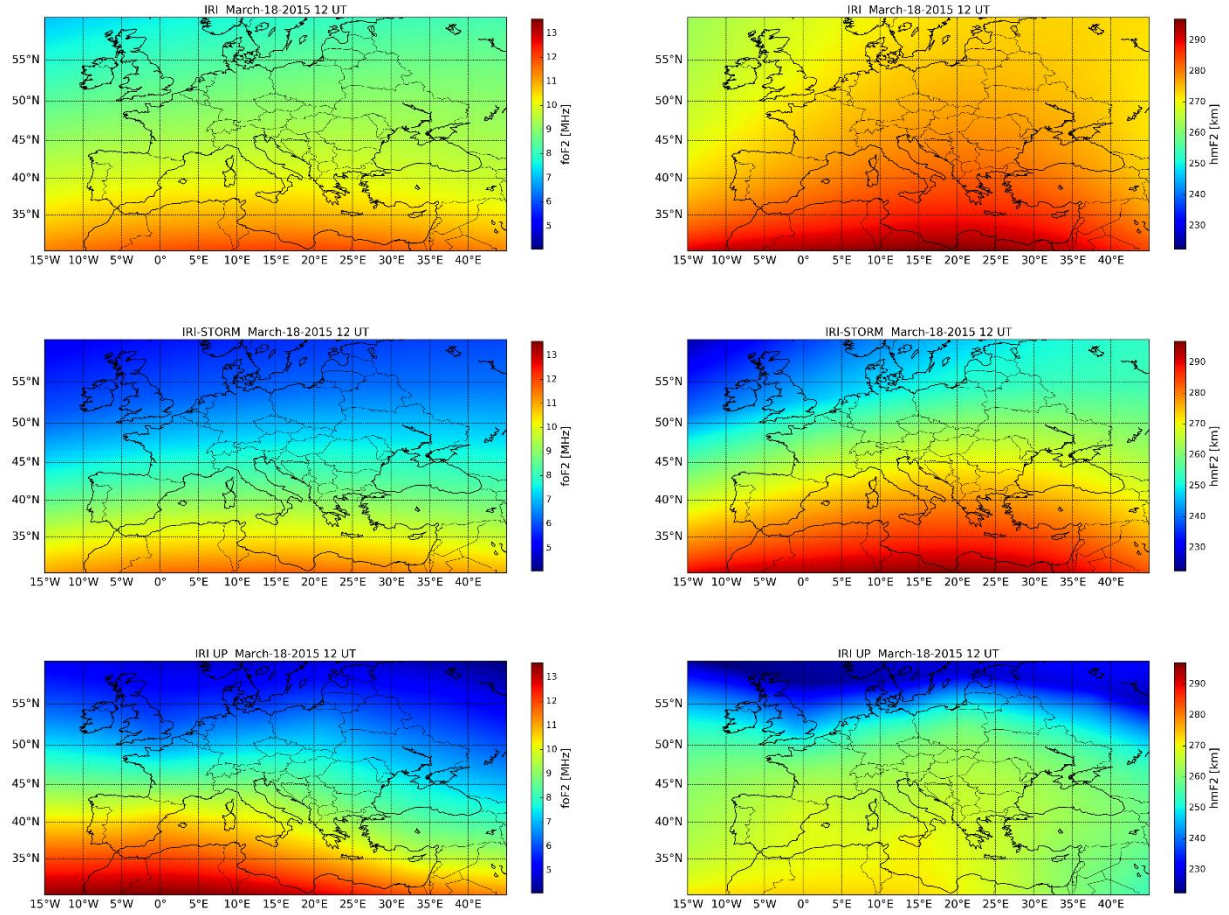
Fig. 11 Same as Fig. 9 but for the disturbed day March 18 2015 (calendar day 77) at 12 UT.

5 Conclusions

This paper, after reviewing methods using effective indices to reliably represent the ionospheric plasma distribution, proposes a method, called IRI UP (International Reference Ionosphere UPdate), to update the IRI model, which is mathematically described and statistically evaluated under a severe geomagnetic event, the St. Patrick storm occurred in March 2015. IRI UP relies on the assimilation of *fo*F2 and *M*(3000)F2 data routinely recorded by a network of ionosonde stations, to calculate updated effective indices $IG_{12\text{eff}}$ and $R_{12\text{eff}}$ at each station of the network; then a universal Kriging method is applied to generate maps of these indices. To accomplish this task, five variogram models have been statistically evaluated; the spherical model and the linear model turn out to be the best choice for $IG_{12\text{eff}}$ and $R_{12\text{eff}}$, respectively. Maps of these updated indices are then used to update the IRI output in terms of *fo*F2 (directly through $IG_{12\text{eff}}$) and *hm*F2 (indirectly through *M*(3000)F2 and *fo*E values, dependent on $R_{12\text{eff}}$, and *fo*F2 values, dependent on $IG_{12\text{eff}}$). The IRI UP model has been tested by comparing its output with IRI (storm option on) and IRTAM. The statistical analysis show that IRI UP for *fo*F2 has the best precision and accuracy. Concerning *hm*F2, the output of IRI UP is by far better than IRI and similar to that of IRTAM. Analysis of statistical distributions and scatter plots pointed out that IRI UP also for *hm*F2 is precise and accurate. Visual analysis of *fo*F2 and *hm*F2 maps confirms the goodness of the IRI UP method, highlighting its ability to catch rapid and small-scale electron density changes occurring especially under disturbed conditions, that cannot be seen by IRI.

The method, even though promising, has been tested by considering only a single storm. Since every geomagnetic storm shows very distinctive features from one to another, depending also on the season and on

the level of solar activity in which it occurs, a validation based on a larger database covering several geophysical conditions is needed and is planned in the future, to bring out any weakness not emerged through the analysis here described.

An analysis based on a larger database is also necessary to further test the five variogram models, because their performance might depend on geophysical boundary conditions.

Moreover, a preliminary quality check of effective index maps has been implemented in this work, based on both the ability to perform the experimental variogram fitting procedure and the value of the *scale* parameter of the power variogram model. It is intention of the authors to improve the quality check routine, by considering residuals obtained by comparing the experimental variogram values with the fitted variogram model, in order to obtain a quality index associated to any map.

Finally, the authors think that, after an additional phase of testing, the method here described could be proposed for a real-time monitor of ionospheric plasma over the European region. It is worth noting that in this work the IRI model has been used as climatological background, but any other similar model using as input solar/ionospheric indices in their formulation of ionospheric characteristics, like for instance NeQuick, could be used as background model.

Acknowledgements

References

Araujo-Pradere EA, Fuller-Rowell TJ, Codrescu MV (2002) STORM: An empirical storm-time ionospheric correction model 1. Model description. Radio Sci 37(5). doi:10.1029/2001RS002467

Araujo-Pradere EA, Fuller-Rowell TJ, Bilitza D (2003) Validation of the STORM response in IRI2000. J Geophys Res 108(A3). doi:10.1029/2002JA009720

Astafyeva E, Zakharenkova I, Förster M. (2015) Ionospheric response to the 2015 St. Patrick's Day storm: A global multi-instrumental overview. J Geophys Res 120(10), 9023-9037. doi:10.1002/2015JA0262

Barabashov BG, Maltseva O, Pelevin O (2006) Near real time IRI correction by TEC-GPS data. Adv Space Res 37, 978-982. doi:10.1016/j.asr.2006.02.008

Belehaki, A, Cander L, Zolesi B, Bremer J, Juren C, Stanislawska I, Dialetis D, and Hatzopoulos M (2005) DIAS Project: The establishment of a European digital upper atmosphere server. J Atmos Solar Terr Phys 67(12), 1092–1099. doi: 10.1016/j.jastp.2005.02.021

Bilitza D, Sheikh M, Eyfrig R (1979) A global model for the height of the F2-peak using M3000 values from the CCIR numerical map. Telecommun J 46, 549-553

Bilitza D (1990) International Reference Ionosphere 1990. NSSDC/WDC-A-R&S 90-22.

Bilitza D, Bhardwaj S, Koblinsky C (1997) Improved IRI predictions for the GEOSAT time period. Adv Space Res 20, 9, 1755-1760, doi:10.1016/S0273-1177(97)00585-1

Bilitza D (2003) International Reference Ionosphere 2000: Examples of improvements and new features. Adv Space Res 31(3), 757-767. doi:10.1016/S0273-1177(03)00020-6

Bilitza D, McKinnell LA, Reinisch B, Fuller-Rowell T (2011): The International Reference Ionosphere today and in the future. J Geod 85, 909-920. doi:10.1007/s00190-010-0427-x

Bilitza D, Altadill D, Zhang Y, Mertens C, Truhlik V, Richards P, McKinnell LA, Reinisch B (2014) The International Reference Ionosphere 2012 – a model of international collaboration. J Space Weather Space Clim 4, A07. doi:10.1051/swsc/2014004

Bradley PA, Stanislawska I, Juchnikowski G (2009) Options for mapping foF2. Adv Space Res 43, 1776-1779. doi:10.1016/j.asr.2008.09.028

Buonsanto MJ (1999) Ionospheric stroms – a review. Space Sci Rev 88, 563-601

Carter BA, Yizengaw E, Pradipta R, Retterer JM, Groves K, Valladares C, Caton R, Bridgwood C, Norman R, Zhang K (2016) Global equatorial plasma bubble occurrence during the 2015 St. Patrick's Day storm. J Geophys Res 121(1), 894-905. doi:10.1002/2015JA022194

Caruana J (1989) The IPS monthly T index. Solar-Terrestrial prediction: Proceedings of a workshop at Leura, Australia 2, 257-261

Chapman S (1930) The absorption and dissociative or ionizing effect of monochromatic radiation in an atmosphere on a rotating earth. Proc Phys Soc 46, 26-45

Davis J (1986): Statistics and Data Analysis in Geology. John Wiley & Sons publisher.

De Michelis P, Consolini G, Tozzi R, Marcucci MF (2016) Observations of high-latitude geomagnetic field fluctuations during St. Patrick's Day storm: Swarm and SuperDARN measurements. Earth Planets Space 68(105), 1-16. doi:10.1186/s40623-016-0476-3

Dmitriev AV, Suvorova V, Klimenko MV, Klimenko VV, Ratovsky KG, Rakhmatulin RA, Parkhomov VA (2017) Predictable and unpredictable ionospheric disturbances during St. Patrick's Day magnetic storms of 2013 and 2015 and on 8–9 March 2008. J Geophys Res Space Phys, 122, 2398–2423, doi:10.1002/2016JA023260.

Dudeney JR (1983) The accuracy of simple methods for determining the height of the maximum electron concentration of the F2-layer from scaled ionospheric characteristics. J Atm Terr Phys 45(8/9), 629-640. doi: 10.1016/S0021-9169(83)80080-4

Fuller-Rowell TJ, Codrescu MV, Araujo-Pradere E, Kutiev I (1998) Progress in developing a storm-time ionospheric correction model. Adv Space Res 22(6), 821-827. doi:10.1016/S0273-1177(98)00105-7

Galkin IA, Khmyrov GM, Kozlov AV, Reinisch BW, Huang X, Paznukhov VV (2008) The ARTIS 5. Radio Sounding and Plasma Physics. AIP Conf Proc 975, 150-159

Galkin IA, Reinisch BW, Huang X, Bilitza D (2012) Assimilation of GIRO data into a real-time IRI. Radio Sci 47, RS0L07. doi:10.1029/2011RS004952

Grynyshyna-Poliuga O, Stanislawska I, Swiatek A (2014) Regional ionosphere mapping with kriging and B-spline methods. Chapter 11 in the book "Mitigation of Ionospheric Threats to GNSS: an Appraisal of the Scientific and Technological Outputs of the TRANSMIT Project" edited by Riccardo Notarpietro, Fabio Dovis, Giorgiana De Franceschi and Marcio Aquino, INTECH, 135-147

Habarulema JB, Ssessanga N (2016) Adapting a climatology model to improve estimation of ionosphere parameters and subsequent validation with radio occultation and ionosonde data. Space Weather 15, doi:10.1002/2016SW001549

Hernandez-Pajares M, Juan JM, Sanz J, Bilitza D (2002) Combining GPS measurements and IRI model values for space weather specification. Adv Space Res 29(6), 949-958. doi:10.1016/S0273-1177(02)00051-0

Houminer Z, Soicher H (1996) Improved short-term predictions of foF2 using GPS time delay measurements. Radio Sci 31(5), 1099-1108. doi:10.1029/96RS01965

ITU-R (2009) ITU-R reference ionospheric characteristics. Recommendation ITU-R P.1239-2

Jones WB, Gallet RM (1962) Representation of diurnal and geographical variations of ionospheric data by numerical methods. Telecommun J 29, 129-149

Jones WB, Graham RP, Leftin M (1969) Advances in ionospheric mapping by numerical methods. ESSA Technical Report ERL107-ITS75, US Department of Commerce, Boulder, Colorado, USA

Kitanidis PK (1997) Introduction to geostatistics: application to hydrogeology. Cambridge University Press.

Klimenko MV, Klimenko VV, Zakharenkova IE, Cherniak IV (2015) The global morphology of the plasmaspheric electron content during Northern winter 2009 based on GPS/COSMIC observation and GSM TIP model results. Adv Space Res 55, 2077-2085. doi:10.1016/j.asr.2014.06.027

Komjathy A, Langley R (1996) Improvement of a Global Ionospheric Model to Provide Ionospheric Range Error Corrections for Single-frequency GPS Users. Proceedings of the 52nd Annual Meeting of The Institute of Navigation, Cambridge, MA, June 1996, 557-566

Liu RY, Smith PA, King JW (1983) A new solar index which leads to improved foF2 predictions using the CCIR Atlas. Telecommun J 50, 408-414

Liu RY, Quan KH, Dai KL (1994) A corrected method of the international reference ionosphere to be used in Chinese region. Chin J Geophys (in Chinese) 37(4), 422-432

Liu RY, Liu GH, Wu J, Zhang BC, Huang JY, Hu HQ, Xu ZH (2008) Ionospheric foF2 reconstruction and its application to the short-term forecasting in China region. Chin J Geophys 51(2), 206-213

Maltseva OA, Zhbankov GA, Trinh Quang T (2010) Improvement of the real time total electron content based on the International Reference Ionosphere model. Adv Space Res 46, 1008-1015. doi:10.1016/j.asr.2010.06.011

Matheron G (1963) Principles of geostatistics. Economic geology 58, 1246-1266

McBratney AB, Webster R (1986) Choosing functions for semi-variograms of soil properties and fitting them to sampling estimates. J Soil Sci 37, 617-639

Migoya-Orué Y, Nava B, Radicella S, Alazo-Cuartas K (2015) GNSS derived TEC data ingestion into IRI 2012. Adv Space Res 55(8), 1994-2002. doi:10.1016/j.asr.2014.12.033

Mikhailov AV, Mikhailov VV (1995) A new ionospheric index MF2. Adv Space Res 15(2), 93-97. doi:10.1016/S0273-1177(99)80050-7

Minnis CM (1955) A new index of solar activity based on ionospheric measurements. J Atm Terr Phys 7, 310-321. doi:10.1016/0021-9169(55)90136-7

Mirò Amarante G, Cueto Santamarìa M, Alazo K, Radicella SM (2007) Validation of the STORM model used in IRI with ionosonde data. Adv Space Res 39, 681-686. doi:10.1016/j.asr.2007.01.072

Nava B, Coisson P, Amarante GM, Azpiliculeta F, Radicella SM (2005) A model assisted ionospheric electron density reconstruction method based on vertical TEC data ingestion. Annals of Geophys 48(2), 313-320. doi:10.4401/ag-3203

Nava B, Rodríguez-Zuluaga J, Alazo-Cuartas K, Kashcheyev A, Migoya- Orué Y, Radicella SM, Amory-Mazaudier C, Fleury R (2016) Middle-and low-latitude ionosphere response to 2015 St. Patrick's Day geomagnetic storm. J Geophys Res 121(4), 3421-3438. doi:10.1002/ 2015JA022299

Nava B, Radicella SM, Leitinger R, Coisson P (2006) A near-real-time model-assisted ionosphere electron density retrieval method. Radio Sci 41, RS6S16. doi:10.1029/2005RS003386

Nava B, Coisson P, Radicella SM (2008) A new version of the NeQuick ionosphere electron density model. J Atm Sol Terr Phys 70, 1856-1862. doi:10.1016/j.jastp.2008.01.015

Nava B, Radicella SM, Azpiliculeta F (2011) Data ingestion into NeQuick 2. Radio Sci 46, RS0D17. doi:10.1029/2010RS004635

Olea RA (1974) Optimal contour mapping using universal kriging. J Geophys Res 79 (5), 695-702

Oliver MA, Webster R (1990) Kriging: A method of interpolation for geographical information systems. Int J Geogr Inf Syst 4(3), 313-332

Olwendo OJ, Cesaroni C (2016) Validation of NeQuick 2 model over the Kenyan region through data ingestion and the model application in ionospheric studies. J Atm Sol Terr Phys 145, 143-153. doi:10.1016/j.jastp.2016.04.011

Orus R, Hernandez-Pajares M, Juan JM, Sanz J (2005) Improvement of global ionospheric VTEC maps by using kriging interpolation technique. J Atm Sol Terr Phys 67(16), 1598-1609. doi:10.1016/j.jastp.2005.07.017

Ovodenko VB, Trekin VV, Korenkova NA, Klimenko MV (2015) Investigating range error compensation in UHF radar through IRI-2007 real-time updating: Preliminary results. Adv Space Res 56 (5), 900-906, doi: 10.1016/j.asr.2015.05.017

Pezzopane M, Scotto C (2005) The INGV software for the automatic scaling of foF2 and MUF(3000)F2 from ionograms: A performance comparison with ARTIST 4.01 from Rome data. J Atm Sol Terr Phys 67(12), 1063-1073. doi:10.1016/j.jastp.2005.02.022

Pignalberi A, Pezzopane M, Tozzi R, De Michelis P, Coco I (2016) Comparison between IRI and preliminary Swarm Langmuir probe measurements during the St. Patrick storm period. Earth, Planets and Space 68(93). doi:10.1186/s40623-016-0466-5

Radicella SM, Leitinger R (2001) The evolution of the DGR approach to model electron density profiles. Adv Space Res 27(1), 35-40. doi:10.1016/S0273-1177(00)00138-1

Reinisch BW, Galkin IA (2011) Global Ionospheric Radio Observatory (GIRO). Earth Planets Space 63, 377–381. doi:10.5047/eps.2011.03.001

Rush CM, Fox M, Bilitza D, Davies K, McNamara L, Stewart FG, PoKempner M (1989) Ionospheric mapping – an update of foF2 coefficients. Telecommun J 56, 179-182

Samardjiev T, Bradley PA, Cander L, Dick MI (1993) Ionospheric mapping by computer contouring techniques. Electron Lett 29(20), 1794-1795

Secan JA, Wilkinson PJ (1997) Statistical studies of an effective sunspot number. Radio Sci 32(4), 1717-1724. doi:10.1029/97RS01350

Spogli L, Cesaroni C, Di Mauro D, Pezzopane M, Alfonsi L, Musicò E, Povero G, Pini M, Dovis F, Romero R, Linty N, Abadi P, Nuraeni F, Husin A, Minh LH, Tran TL, The VL, Pillat VG, Floury N (2016) Formation of ionospheric irregularities over Southeast Asia during the 2015 St. Patrick's Day storm. J Geophys Res 121(12), 12211-12233. doi:10.1002/2016JA023222

Stanislawska I, Juchnikowski G, Cander L (1996a) The kriging method of ionospheric parameter foF2 instantaneous mapping. Ann of Geophys 39(4), 845-852. doi:10.4401/ag-4007

Stanislawska I, Juchnikowski G, Cander L (1996b) Kriging method for instantaneous mapping at low and equatorial latitudes. Adv Space Res 18(6), 217-220. doi:10.1016/0273-1177(95)00927-2

Stanislawska I, Juchnikowski G, Cander L, Ciraolo L, Bradley PA, Zbyszynski Z, Swiatek A (2002) The kriging method of TEC instantaneous mapping. Adv Space Res 29(6), 945-948. doi:10.1016/S0273-1177(02)00050-9

Tsagouri I, Zolesi B, Belehaki A, Cander L (2005) Evaluation of the performance of the real-time updated simplified ionospheric regional model for the European area. J Atm Sol Terr Phys 67, 1137-1146. doi:10.1016/j.jastp.2005

Wang S, Liu W, Jiao P, Kong Q (2010) A study on the ionospheric parameter foF2 instantaneous mapping based on equivalent sunspot number. IEEE Conference Publications, 407-410

Zhong J, Wang W, Yue X, Burns AG, Dou X, Lei J (2016) Long-duration depletion in the topside ionospheric total electron content during the recovery phase of the March 2015 strong storm. J Geophys Res 121(5), 4733-4747. doi:10.1002/2016JA022469

Zolesi B, Cander L, De Franceschi G (1993) Simplified ionospheric regional model for telecommunication applications. Radio Sci 28(4), 603-612. doi:10.1029/93RS00276

Zolesi B, Belehaki A, Tsagouri I, Cander L (2004) Real-time updating of the Simplified Ionospheric Regional Model for operational applications. Radio Sci 39, RS2011. doi:10.1029/2003RS002936

Zolesi B, Cander L (2014) Ionospheric Prediction and Forecasting. Springer Geophysics